

Self-consistent modelling of cyclic loading and relaxation in austenitic 316H stainless steel

Markian P. Petkov^{a†}, Jianan Hu^{a, b}, Alan C.F. Cocks^a

^a *Department of Engineering Science, University of Oxford, OX1 3PJ, UK*

^b *Sente Software, Guildford, GU2 7YG, UK*

Keywords: *relaxation, cyclic, crystal plasticity, self-consistent, strain dwells, stress redistribution*

ABSTRACT

In the present study the Hu-Cocks micromechanical model [1,2] for dislocation-obstacle interactions, implemented in a crystal plasticity self-consistent model, is employed to simulate thermo-mechanical histories typical for AGR nuclear plants in order to assess the implications of creep-fatigue interactions in 316H stainless steel. Their physical model is enhanced by including the effect of dynamic recovery, which introduces a new material parameter - the annihilated segment length ΔL_r . The full model contains five independent material parameters; other parameters are prescribed by the fundamental physics of inelastic deformation processes. Having calibrated the model, we explore its ability to predict material response under complex loading histories to provide insight into the physical phenomena controlling cyclic-creep interactions. Introduction of strain dwells during cyclic loading results in an increase of the extent of relaxation with increasing number of cycles, but histories with dwells at different strain levels indicate that relaxation is strongly dependent on initial stress and level of constant strain. Predictions of history-dependent relaxation demonstrate that the least stress relaxation results after creep into the secondary regime and the largest stress drop results during hold-dwells after monotonic elastic-plastic loading, with the cyclic-dwell history behaviour laying in between these two. Both prior cycling and the generated residual stress field are found to affect the primary creep regime under hold-stress dwells. These results are consistent with experimental observations; this demonstrates that deformation response is dependent on both the evolution of microstructural state and redistribution of stress between the grains of the polycrystalline aggregate.

[†] Corresponding author. Tel.: +44 (0) 1865 283245

Email address M. Petkov: markian.petkov@eng.ox.ac.uk

A.C.F. Cocks: alan.cocks@eng.ox.ac.uk

J. Hu: jianan.hu@sentesoftware.co.uk

NOMENCLATURE

b	Burger's vector
c	Concentration of solute atoms
D_c	Core diffusion
E	Young's modulus
F_{sol}	Strength of solute drag
ΔF_0	Activation energy for bypassing
G	Shear modulus
ΔG^*	Thermal activation energy
j_s, j	Fitting parameters - hardening
k	Boltzmann constant
L_d, L_p, L_s	Spacing of dislocation junctions, precipitates and solutes
ΔL_r	Annihilated dislocation segment length
N_d, N_0	Current and initial number density of dislocation junctions
p, q	Flow rule exponents
t	Time
T, T_m	Temperature, melting temperature
ν	Poisson's ratio
W_c	Fitting parameter – static recovery
$\alpha_0, \alpha_d, \alpha_s$	Obstacle bypassing, dislocation junction, solute strength
$\gamma, \dot{\gamma}, \dot{\gamma}_0$	Resolved shear strain, strain rate and reference shear strain rate
$\varepsilon, \varepsilon_{pl}$	Total and plastic strain
σ, σ_{max}	Stress tensor, Maximum saturated stress
$\tau, \tau_{cr}, \bar{\tau}_m^r$	Resolved and critical resolved shear stress; Type III residual stress
τ_d, τ_p, τ_s	Internal resistance - dislocation, precipitates, solutes

1. INTRODUCTION

The current Type II Advanced Gas-Cooled Nuclear Reactors (AGR) operated by EDF Energy in the UK are approaching their design life of 30 years. Due to economic factors, such as generation of revenue from continuing operation of existing plants before the introduction of the next generation of reactors,

and environmental reasons, e.g. decreasing CO₂ emissions by using alternatives to fossil fuels, the current energy strategy in the UK is to extend the life of the current nuclear plants. In order to achieve this, more detailed understanding of the deformation and failure behaviour of critical components is required. During operation of a nuclear plant, a component can experience complex mechanical and thermal histories [3]. At the elevated temperatures of operation, life-limiting issues become the time-dependent inelastic deformation of components, together with subsequent creep fracture due to the steady accumulation of damage. Austenitic stainless steel Type 316H is used mainly in the boiler section of a typical AGR power plant with the majority of components operating at temperatures in the range 470-650°C and stresses of the order 100-300 MPa [4]. Empirical models, such as the RCC-MR equations [5], are currently used to predict creep deformation, but discrepancies arise between experiments and model predictions. In order to understand better the deformation and failure of 316H and provide guidelines for improvement of existing models and assessments more sophisticated physical modelling of the material is required.

Components operating at elevated temperatures can fail as a result of excessive inelastic deformation (global strains in boiler components are typically limited to 1%, with local strains allowed to reach 5%) or due to creep fracture, arising from the nucleation, growth and coalescence of intergranular cavities [6]. Thermal stresses tend to be more significant than those induced by mechanical loading. For displacement-controlled loading conditions of this type the UK R5 assessment procedure uses a ductility exhaustion approach [7]. When using these procedures, it is important to have an accurate assessment of the accumulation of creep strain over a typical loading cycle in order to determine the amount of damage accumulated over a cycle, which requires accurate and robust constitutive models for the inelastic deformation experienced during the life of a component. In this paper we focus on the development of physically-based models that can be used to predict the deformation response over the types of loading histories experienced in the current fleet of AGRs. These models are relevant to the

prediction of failure due to excessive creep deformation and the accumulation of damage through a ductility exhaustion approach.

A typical major cycle experienced by a material element in a boiler component might consist of a strain-controlled cycle with a dwell either at the peak or an intermediate location in the cycle, during which creep strain is accumulated and the stress relaxes. Recently, Hu and Cocks [2] developed a self-consistent model (SCM) for the elasto-viscoplastic behaviour of 316H stainless steel which models the evolution of internal material state (i.e. dislocation structure) and grain-to-grain variations of the internal residual stress state, both of which play important roles in determining the macroscopic inelastic response. Their model was developed for transient plastic and creep problems and for loading conditions that involve a small number of cycles. Here we revisit this model and make changes which allow for an accurate description of the material response during the type of thermo-mechanical loading histories described above. This involves introducing terms for dynamic recovery and re-evaluating how the model is calibrated to simultaneously provide an accurate description of the deformation response during both constant load creep and relaxation tests. The final model contains five parameters that need to be fit to data; because of its physical basis, all other parameters in the model are determined from fundamental physical considerations – such as the length of Burger’s vector for the studied material. We use four different experiments to determine the five unknown parameters – (i) monotonic loading at low temperature into the plastic regime; (ii) strain controlled cyclic loading at low or high temperatures up to saturation of the cyclic stress-strain curve; (iii) rapid loading at a temperature within the range of interest (typically 525 to 600°C) followed by a period of creep at constant load; and (iv) the loading of (iii) at the end of which the strain is fixed and the stress is allowed to relax. The degree to which the resulting calibrated model predicts the material response under more complex loading histories typical of those experienced in an AGR is explored and evaluated. The focus of the current paper is on the behaviour of a particular engineering alloy (Type 316H stainless steel), but the model and fitting procedure can be

applied to any polycrystalline material – adjustments to the embedded crystal plasticity model might need to be made to capture the major internal physical processes that dominate in the material of interest. It should be noted that here we do not aim to devise models which can be applied directly to component assessment. The focus of the present article is to combine models describing the general physics of the deformation mechanisms at the microscale within a framework capturing the stress redistribution processes at the mesoscale, and through capturing the correct trends and magnitude in predictions, independent of free parameters, to explain observations on the deformation response through the underlying physics and interactions between processes. The relevance of the present work to actual components stems from the insights provided by this model into such micromechanical processes, in addition to the available experimental database, and their influence on deformation response during complex loading histories, common to AGR nuclear plants. To make more feasible the statistical assessment of real-life components where the majority of models are phenomenological, those insights into the interactions between micromechanical processes can be translated to assessment approaches in industry in order to enrich the phenomenological frameworks and potentially allow for more accurate predictions.

In the following section we provide a more detailed overview of the material response under cyclic loading and during relaxation and how these are influenced by prior plastic deformation. The self-consistent model of Hu and Cocks [2] is described in Section 3. Modifications to the model are then introduced to account for dynamic recovery. The remaining sections focus on the application of the model to the full range of loading histories described above.

2. MATERIAL RESPONSE DURING CYCLIC LOADING AND RELAXATION

2.1 CYCLIC DEFORMATION

Understanding cyclic deformation is important in nuclear power plants, where the major cycle is due to periodic shutdowns for scheduled maintenance. During cycles of this type the material experiences complex deformation histories which result in both hardening and dynamic and static recovery [8] of the dislocation structure with accumulation of cycles until saturation of the stress-strain response is reached after a number of cycles [9]. Cyclic deformation in a continuum plasticity sense is commonly described through isotropic and kinematic hardening [9]. A widely-used material model to describe cyclic behaviour is the Chaboche-Lemaitre unified viscoplasticity model [10,11]. The model has been used for prediction of strain- and stress-controlled cyclic deformation of austenitic 316 stainless steel providing accurate predictions of deformation response, e.g. [12]. Cyclic deformation is known to affect the subsequent creep [13], relaxation and creep failure response of materials and studies have been conducted to investigate such dependencies using the Chaboche model [14]. However, the large number of fitting parameters and empirical nature of the model suggest that physically-based modelling of cyclic deformation and cyclic behaviour with relaxation or creep dwells is required to accurately predict subsequent creep deformation. In a physical sense, however, the complex deformation behaviour is a result of the change in internal resistance to dislocation motion, e.g. microstructural changes, change in obstacle spacing, etc., and the evolution of residual stress fields within the polycrystal. The focus of this study is to capture the deformation response during cyclic loading by considering those physical processes controlling the macroscopic behaviour. The evolution of internal state – hardening and softening behaviour due to changes in the dislocation obstacle network – and changes in the stress field at the grain scale have been studied within crystal plasticity frameworks by Bruzzi et al. [15] and Turkmen et al. [16] under strain- and stress-controlled loading histories, respectively. Both studies

identified the importance of elastic anisotropy and crystallographic orientation of individual grains on the macroscopic stress-strain response during cyclic loading. The coupling between the elastic anisotropy of the crystal and its plastic anisotropy, associated with the micromechanical deformation mechanisms at the slip system level, were observed to drive the evolution of the local and global mean stress field. Also, in both the empirical Chaboche type models and the crystal plasticity models it is recognised that saturation of the stress-strain response occurs when there is a balance between the rates of hardening and dynamic recovery of the material state. Any physically based or empirical model must contain these elements if it is to fully model the cyclic material response.

2.2 *STRESS RELAXATION*

Many components in power-generating plants experience loading conditions at high temperature which involve displacement-controlled deformation, essentially resulting in creep at constant strain rather than stress [17]. At constant total strain, i.e. $\dot{\epsilon}_t = 0$, relaxation of stress occurs due to accumulation of creep strain and a concomitant reduction of elastic strain. A major focus in recent years has been the prediction of relaxation behaviour from forward creep (creep at constant stress) models. Accurate predictions are usually achieved by using creep models with a large number of fitting parameters [18,19] or “back stress” terms (e.g. $(\sigma - \sigma_{back})^n$) whose physical origin is not yet fully understood [20–22]. Predicting relaxation of 316H stainless steel from forward creep has mainly been carried out through the RCC-MR equations [21]. Accurate predictions using such empirical models for creep are possible, but this generally requires fitting the model to relaxation rather than creep data. This also requires a large number of free parameters and does not aid the physical understanding of the relationship between creep and relaxation. Phenomenological models often use an internal stress term which attempts to describe the internal friction in the lattice present during deformation. Such a phenomenological model used in [5] combines a model proposed by Feltham [23] with a “back-stress” term - the predictions agree well with experimental data for 316H stainless steel at 550°C. Other more successful attempts approach the

problem by splitting the initial rapid decrease of stress, relating it to short-term plasticity, and the long-term steady-state stress drop [24]. It was observed that stress relaxation at short times is better described by the first term which suggests that initial stages of relaxation during creep are determined by thermally-activated glide mechanisms. The major part of the total relaxed stress during creep relaxation occurs during the initial stages, hence the process should be considered and modelled in detail. The observations of a two-stage relaxation process agree with the description of initial transient behaviour given by Hart and Solomon [25] suggesting that the initial stage of relaxation might be due to inelastic recovery, therefore consideration on the physical description of glide and climb modes of deformation should be made separately. The initial rate-controlling mechanism in [25] was assumed to be related to recovered inelastic strain which is recoverable upon release of the stress. Moreover, larger amounts of relaxed stress at a higher constant strain were recorded during the transient period of a relaxation test [17]. This would further suggest that the initial stages of relaxation are controlled by glide of mobile dislocations. Similar observations were made during LCF tests on Type 316 stainless steel between 500°C and 650°C [26], where it was observed that the higher the amplitude of the initial strain at the start of a hold, the larger the amount of stress relaxation during the transient period.

Phenomenologically, the creep part of the stress relaxation at longer times is often related to creep recovery at high temperature with the rate-controlling mechanism being dislocation climb [27,28]. It is important to note, however, that in Type 316 stainless steel the creep-controlling mechanisms in the temperature range between 500-650°C can change significantly [21,22,29,30]. An example of such behaviour is the strong effect of solute drag [29] at temperatures below 550°C and strain-rates below 10^{-6} s^{-1} . During stress relaxation at longer times local and global climb mechanisms may also have a significant effect, compared to their effect during forward creep, as suggested in [30]. The initial microstructural morphology of a solution-treated 316H alloy will also be of importance when considering stress relaxation over prolonged periods, since the creep resistance of the alloy has been observed to vary

significantly with formation and evolution of different precipitate complexes [29,31]. The relaxation behaviour has also been observed to depend on prior deformation history [22]. Since primary and secondary creep regimes are observed to depend on the evolution of internal state and residual stress field [32,33], observations on modelling relaxation from forward creep laws suggest that more accurate predictions require a physical state-variable approach within a framework that also captures stress redistribution between grains during the relaxation process. The evolution of internal state of the material is typically modelled through semi-empirical constitutive models based on continuum plasticity, e.g. [10,34], however, under complex loading histories such models require a large number of fitting parameters to produce accurate predictions. The models used in continuum plasticity are simplified functions predicting general trends in response, however, these models do not capture the detailed physics behind the deformation behaviour. Continuum plasticity is also unable to capture local interactions between anisotropic crystals within a polycrystalline aggregate which has been observed to affect the macroscopic response [19]; on the contrary crystal plasticity frameworks can allow for such local behaviour to be captured [35]. Dislocation obstacle density-based mechanistic models, such as that developed by Kocks and co-workers [36–38], provide a physically-rich theoretical framework than phenomenological models, and have provided the physical basis and motivation for the development of the multi-scale SCM developed by Hu and Cocks [2,29], which is further enhanced as part of this study. Physically based modelling frameworks, such as self-consistent models (SCM) and crystal plasticity finite elements (CPFE) approaches, allow physical models of deformation to be applied at the grain scale, with the mechanics framework providing information about the local grain-to-grain interactions and their effects on the global deformation response. Self-consistent modelling of stress relaxation in stainless steels with a physical constitutive model carried out by Wang et al. [19,39] showed the importance of the evolution of internal material state and residual stress, providing a possible explanation of the “back stress” term. Dunne et al. [40] investigated cold-dwells in Ti-alloys through a physical CPFE model,

noting the importance of local residual stress evolution in determining the macroscopic response during a strain-dwell.

2.3 *CYCLIC-CREEP INTERACTIONS*

Understanding the effects of prior cyclic plasticity on subsequent creep response during strain- or stress-controlled dwells is of importance to assessing the deformation and damage response of components in nuclear power plants which undergo complex thermo-mechanical loading histories [41]. Previous studies of creep-fatigue interactions in austenitic stainless steel demonstrate that the amount of creep strain accumulated during a dwell after pre-straining decreases significantly as a result of the cyclic hardening of the microstructure [13,42]. It is also observed that this reduction in creep strain is manifested in the decrease of both primary and secondary creep rates, as described by Kikuchi and Ilschner [42]. Studies by Ajaja and Ardell [43] and Fookes et al. [41], however, demonstrate that pre-straining can have little or no effect on the secondary creep strain rate which is contradictory to the observations reported in [42]. Experimental studies on the changes in stress relaxation response during strain dwells introduced at different positions in the stress-strain cycle have also been conducted by Fookes et al. [44]. It is shown that the extent of stress relaxation and, respectively, the generation of creep strain during the dwell decreases with increasing number of cycles – this phenomenon is believed to be as a result of the accumulation of larger dislocation densities during subsequent cycles which induces a residual “back” stress in the microstructure [44]. In order for these complex interactions between cyclic and creep deformation to be explained, detailed microstructural analysis and physical models are required to provide additional information of the evolution of the material state. The simplistic models used to replicate and explain the trends observed in studies on creep and relaxation dwells during cyclic loading are unable to fully capture the experimental response. No unified micromechanical models have been employed previously in the literature to explain the experimentally observed differences in creep response after prior cyclic hardening.

In the following sections we modify the Hu and Cocks [2] self-consistent model (SCM) to take into account the effect of dynamic recovery on the crystal level constitutive response and how this influences the macroscopic behaviour under cyclic loading. We also modify the interpretation of terms within the model and how these are determined from experiments, which allows both relaxation and forward creep to be accurately modelled within the same model. These extensions allow the behaviour during stress- and strain-controlled dwells during a cyclic loading history to be investigated. Predictions of a range of complex thermo-mechanical loading scenarios will potentially provide a clearer understanding of the “back stress” term used in phenomenological models, as well as the deformation response during transient and steady-state relaxation periods. Section 3 describes the current Hu and Cocks [1,2] self-consistent model and introduces further enhancements to the model in capturing behaviour during cyclic deformation. A strategy for determining the independent material parameters in the model from a limited series of experiments is also described. Sections 4 and 5 demonstrate the predictive capabilities of the SCM for relaxation and cyclic deformation as separate deformation modes. In Section 6 model predictions for combined relaxation dwells during strain-controlled cyclic loading are reviewed; with the effects of prior plasticity on subsequent constant stress creep dwells briefly examined in Section 7. The results are further discussed and evaluated in Section 8.

3. THE HU-COCKS SELF-CONSISTENT MODEL AND ITS EXTENSION

Hu and co-workers [2,29,45] have developed a physical model of elastic-plastic deformation and forward creep of 316H austenitic stainless steel. The model captures the evolution of microstructure - comprising the dislocation network, distribution of precipitates and concentration of elements in solute complexes - and stress fields in the polycrystalline material aggregate. The constitutive laws are implemented within a self-consistent model (SCM), which captures the deformation of anisotropic grains, represented as inclusions in an infinite elastic matrix. Validation of the present model at the microscale has been carried

in previous work by the authors for the same alloy under both high- and low-temperature loading conditions – residual stresses and microscopic lattice strains for selected grain families captured via neutron diffraction (ND) experiments have been predicted by the model, showing good agreement with data under short- and long-term inelastic loading histories of both ex-service (EX) and solution treated (SA) material [1,2,29]. Here, we do not seek to further calibrate the model and attention is focused on the predicted macroscopic response. The aim is to demonstrate an approach to calibration of a physical multiscale model with a low number of parameters to experimental data in order to make independent predictions of response in more complex loading histories. It is important to note, however, that at present some of the experimental data on macroscopic response under the operating conditions of interest is not present and difficult to obtain.

The model by Hu and Cocks [1,2,29] is based on three different scales – micro-, grain- (or meso-) and macro-scale – and captures the evolution of the distribution of obstacles to dislocation motion in terms of their spacing. A general overview of the model is given in the following subsections; a full description is omitted for brevity and can be found in [2,29,30,46].

3.1 CRYSTAL PLASTICITY FRAMEWORK

The response of the individual anisotropic grains is modelled through crystal plasticity (CP) theory, which is treated within a small-deformation framework, since the SCM developed by Hu and Cocks [2] is built within a framework where lattice rotations are ignored. Petkov et al. [47] have compared predictions using the SCM model with full 3-D large deformation CPFEM simulations and demonstrated that for the range of problems of interest here (macroscopic strains up to 5%) the current small deformation assumption provides an accurate description of the macroscopic response. The plastic strain rate in each crystal can be determined via the CP model by summation of the slip rates on individual slip systems within the crystal. In FCC materials such as 316H, 12 systems are formed from the three $\langle 110 \rangle$

slip directions $\bar{s}^{(\alpha)}$ and four $\{111\}$ slip planes $\bar{n}^{(\alpha)}$ [48]. Hence, by summing the contributions from each slip system, (α) , the plastic strain increment in every grain is obtained by [49,50]:

$$\Delta \varepsilon^{pl} = \sum_{\alpha=1}^{12} \Delta \gamma^{(\alpha)} \text{sym}(\bar{s}^{(\alpha)} \otimes \bar{n}^{(\alpha)}) \quad (1)$$

where the Schmid factor, $\text{sym}(\bar{s}^{(\alpha)} \otimes \bar{n}^{(\alpha)})$, relates the shear strains resolved along each slip system to the plastic strains in the local cartesian coordinate system of the crystal [51]. The flow rule, which describes the evolution of resolved shear strain rate $\dot{\gamma}^{(\alpha)}$ along each slip system is of physical nature, assuming the functional form

$$\dot{\gamma}^{(\alpha)} = \dot{\gamma}_0 g(\Delta F_0, T, \tau^{(\alpha)}, \tau_{cr}^{(\alpha)}) \quad (2)$$

The term ΔF_0 in Eq. 2 represents the required activation enthalpy due to thermal fluctuations for inelastic deformation on a slip system which is added to the external work done to the material via external forces [52]. In the context of crystal plasticity, the external work done is a function of the resolved shear stress on a slip system, $\tau^{(\alpha)}$, and the internal resistance of the slip system to dislocation motion, $\tau_{cr}^{(\alpha)}$. Kocks et al. [52] proposes a physical rate-dependent function for the inelastic slip rate along a slip system which considers the thermal activation process of dislocation glide allowing the system to reach a new plastically-deformed state at a temperature T according to

$$\dot{\gamma}^{(\alpha)} = \dot{\gamma}_0 \exp \left(-\frac{\Delta F_0}{kT} \left(1 - \left| \frac{\tau^{(\alpha)} + (\bar{\tau}_m^r)}{(1 + F_{sol})\tau_{cr}^{(\alpha)}} \right|^{\frac{3}{4}} \right)^{\frac{4}{3}} \right) \text{sgn}(\tau^{(\alpha)}) \quad (3)$$

where $\bar{\tau}_m^r$ is the Type III (micro-) internal residual stress [45], k is Boltzmann constant and $\dot{\gamma}_0$ the reference shear strain rate. The term F_{sol} in Eq. 3 is a thermal solute strengthening term depicting the solute drag process, which results in an enhancement of the critical resolved shear strength and is modelled via the theory suggested by Schmidt and Miller [53,54]. We write ΔF_0 in Eq. 3 in the form [52]

$$\Delta F_0 = \alpha_0 G_0 b^3 \quad (4)$$

where G_0 is the shear modulus at 0 K and α_0 is a dimensionless parameter that scales with the effective shear strength of the obstacles. Frost and Ashby [55] demonstrate that $2 > \alpha_0 > 1$ for strong obstacles (such as precipitates), $\alpha_0 < 1$ for medium obstacles (such as dislocation junctions) and $\alpha_0 \ll 0.2$ for weak obstacles (such as solute atoms). For a mix of obstacles α_0 will lie within this overall range.

In this study of ex-service 316H stainless steel with a pre-existing considerable population of precipitates, F_{sol} is simply set to zero. For a detailed evaluation of the effect of F_{sol} in the self-consistent model, one can refer to [30]. The resolved shear stress on a system is obtained through the outer product of the Schmid tensor and stress tensor as

$$\tau^{(\alpha)} = [\text{sym}(\bar{s}^{(\alpha)} \otimes \bar{n}^{(\alpha)})] : \bar{\sigma} \quad (5)$$

The polycrystalline aggregate is modelled via a self-consistent scheme [2] similar to that proposed by Kroner [56] and Budiansky and Wu [57], which captures the redistribution of intragranular residual stresses and models the global deformation response of material under the assumption that grains are anisotropic inclusions in an isotropic elastic matrix.

3.2 MICROSCOPIC DISLOCATION-BASED STATE VARIABLES

The microscopic part considers the contributions of three dominant obstacles to the internal resistance, τ_{cr} , on each crystallographic plane (see Figure 1). In 316H austenitic stainless steel, the three main groups of obstacles blocking the dislocation motion are forest dislocation junctions, solute atoms and precipitates [30]. The critical resolved shear strength (CRSS) or the internal resistance on a slip system (τ_{cr}) is expressed as a function of the characteristic average spacings of each obstacle family - L_d for dislocation junctions, L_p for intragranular precipitates of $M_{23}C_6$ type, and L_s for discrete solute atoms in the crystal matrix – according to

$$\tau_{cr} = \left(\sqrt{\left(\frac{\alpha_d G b}{L_d} \right)^2 + \left(\frac{\alpha_p G b}{L_p} \right)^2} \right) + \alpha_s G b (c b)^{\frac{1}{2}} \quad (6)$$

where G is shear modulus, and b is the magnitude of Burger's vector [58]. The contributions of forest junctions, precipitates and solute atoms to the internal resistance scale with temperature through the variation of shear modulus, after [55]. It is worth noting that the spacing L_s has been expressed as a function of the concentration c of discrete solute atoms in the alloy [2]. The terms α_p , α_d and α_s in Eq. 6 are dimensionless obstacle strength constants; these are derived from geometrical consideration on the obstacle distribution of each type, together with their effect on dislocation segments which attempt to overcome the obstacle [59].

Division of dislocations into finer segments, as a result of mobile dislocations intersecting forest junctions [30], causes evolution of the dislocation obstacle density N_d . Multiplication of dislocations over a given increment of resolved shear strain $\Delta\gamma$ on a slip plane, which refines the microstructure, results in increments of obstacle density due to self- or latent-hardening within the crystal expressed as

$$\Delta N_{self} = j \Delta\gamma \quad (7)$$

$$\Delta N_{latent} = j_s \Delta\gamma \quad (8)$$

where j_s and j are fitting parameters [2]. Phase transformation processes in solution-treated material are also included in the micromechanical model in order to describe the evolution of solute concentration and precipitates, together with their contributions to the internal resistance, see [29]. In the present study this feature of the response is neglected and will not be considered further here, as the study examines short-term creep behaviour of 316H ex-service samples, where evolution of phases is negligible. The contribution to internal resistance of prismatic dislocation loops, which are punched from the precipitates

as the dislocations bow around them [60], is also captured in the model through the consideration of the internal lattice stress at the slip system level (Type III residual stress) introduced by such loops.

[Figure 1 here]

The thermal recovery of the dislocation network is described by Hu and Cocks [1] assuming that at elevated temperatures long dislocation links grow at the expense of short ones as the result of diffusion of material through the cores of the dislocations. Hence, the full version of the evolution of the state variable can be expressed as

$$\dot{L}_{di} = -\frac{1}{2}L_{di}^3 \left(\frac{j_s}{s} \dot{\gamma}_i + \frac{j}{s(m-1)} \sum_{j \neq i} \dot{\gamma}_j \right) + \frac{W_c D_c G b^5}{kT} \frac{1}{L_{di}^3} \quad (9)$$

where D_c is the core diffusivity, W_c is the controlling free parameter for static recovery and L_{di} is the dislocation junction obstacle mean spacing, illustrated in Figure 2 [30].

[Figure 2 here]

3.3 MICROMECHANICS OF DYNAMIC RECOVERY

Dynamic recovery results from continuous annihilation of dislocation dipoles within the crystal through accumulation of plastic strain; including this feature of the material response is particularly important under cyclic loading [8]. The phenomenon is not yet captured in the multi-scale model, introduced in Section 2, and its incorporation as part of this study enhances the existing framework. Nes et al. [61] suggest that dynamic recovery is a function of dislocation annihilation frequency, strain rate and dislocation density. Their model, however, assumes dislocation cell formation within the grain matrix which is observed in 316H at temperatures $>700^\circ\text{C}$ [30,62], higher than the temperature range of interest for this study. Below the temperature range $625\text{-}650^\circ\text{C}$, at which the model developed here is applied, TEM experimental results on Type 316 and 316H stainless steels demonstrate that formation of distinctive dislocation cells or subgrains during both cyclic and creep deformation histories is not

pronounced [62–67] due to the presence of uniformly-dispersed intragranular precipitates of $M_{23}C_6$ type, hence, the present framework does not incorporate any models of this physical process. Kocks [37] suggests a simpler model of dynamic recovery based on the probability that a dislocation segment length (ΔL_r) is annihilated in a unit volume as a function of accumulated obstacle density with an increment of the resolved inelastic shear strain $\Delta\gamma$. (Figure 3).

[Figure 3 here]

Applied at the slip plane level, the model by Kocks [37] agrees with the state variable employed in the multi-scale model (spacing of dislocation obstacles, L_{di} , or their number density, N_d) and takes the form

$$\Delta N_{di} = -\frac{\Delta L_r}{b} N_{di} \Delta\gamma \quad (10)$$

Eq. 10 provides an additional term to the evolution of density of obstacles to dislocation motion, which acts to increase the spacing between dislocation junctions with an increment of resolved shear strain. The purpose of including dynamic recovery is to provide a more accurate description of the physical processes behind the evolution of internal state during cyclic loading.

3.4 PROCEDURES FOR FITTING EXPERIMENTAL DATA

The above model contains a number of parameters that need to be fit to experimental data. These relate to: (i) the initial yield strength, determined from the initial spacing of the forest junctions L_d , precipitates L_p , and concentration c of solute atoms, through Eq. 6; ii) self/latent hardening, represented by the parameters, j and j_s in Eqs. 7 and 8; iii) static recovery, whose rate is determined by the dimensionless quantity W_c in Eq. 9; iv) activation energy for thermal activation of dislocations over obstacles, governed by the dimensionless quantity α_0 in Eq. 4; and v) dynamic recovery, which is determined by the characteristic length for annihilation of dislocations ΔL_r , in Eq. 10. In their original model Hu and Cocks [1,2,29] considered only plastic deformation under monotonically increasing load, with a single reversal

of load, and creep at constant load for moderate levels of inelastic strain. Under these conditions, dynamic recovery does not play a significant role in determining the response and was ignored in their model. The solute concentration and mean spacing of precipitates were determined from a knowledge of the alloy composition and from micrographs and energy-dispersive X-ray spectroscopy (EDX) studies. The degree of latent hardening, represented by the ratio j_s/j , was set to 1.4 based on the results of discrete dislocation dynamics simulations [45]. The initial yield strength and hardening behaviour are then determined by the initial value of L_d , which is related to the initial density of pinning points N_0 (which in turn depends on the initial dislocation density) and the way in which it evolves, which is determined by j . These parameters were chosen to provide the best fit to experimental data. The creep response is determined by the parameters α_0 for thermally-activated glide and W_c for static recovery. At elevated temperatures the precipitate size (and the type of precipitates) can evolve which also affects the solute concentration in the matrix. Evolution laws for L_p and c are provided in [29] based on physical models of the nucleation and growth of precipitates. Hu and Cocks [1] only considered short term exposure at elevated temperature during which time there is minimal evolution of the precipitate distribution, and they took L_p and c to be constant during the duration of the experiments they evaluated. In their fit of experimental data for the creep response they set α_0 equal to 1, which is a simple numerical average of the values of α for the different types of obstacles, and determined W_c by fitting the experimental creep data.

Here, we are interested in modelling both creep and relaxation behaviour, which are both determined by α_0 and W_c (once the time dependent plastic response is calibrated). In the next section we re-evaluate the assumption of Hu and Cocks [2,30] that $\alpha_0 = 1$ and demonstrate that both α_0 and W_c need to be treated as independent fitting parameters, with the constraint that α_0 must be in the physical range $0.1 < \alpha_0 < 2$. In Section 5 we consider the material response under cyclic loading. A major conclusion of these sections is that we can completely calibrate the model from 4 independent tests, namely: i) uniaxial loading at room temperature; ii) a strain-controlled cyclic loading test at room temperature; iii) a standard

creep test at constant load; and iv) a relaxation test, following monotonic loading up to the initial stress state. Having calibrated the model in this way, we examine the ability of the model to predict the material response for more complex loading histories.

4. RELAXATION MODELLING

This section presents studies using the multi-scale self-consistent model introduced in Section 3 and focuses on stress relaxation of 316H at high temperature. The experimental data during both monotonic elastic-plastic loading and forward creep has been provided by EDF Energy. Due to the significant variation in deformation response across different casts of 316H, this study focuses on ex-service ($\sim 65 \times 10^3$ hours) Cast 69431. The chemical composition of the material is shown in Table 1. The texture in Type 316H polycrystalline material employed in previous studies, e.g. [2,68], was found to be weak (approximately random, see Figure 5), hence the material here is treated as a globally-isotropic body. The physical phenomena considered in the micromechanical model used in the following sections are illustrated in Figure 4.

[Figure 4 here]

In this part of the study we predict relaxation using the original SCM developed by Hu and Cocks [2,30], with the parameters which they determined to provide an accurate fit for forward creep, with the assumption that $\alpha_0 = 1$, at the temperature and stress level of interest. We then assess the role of the activation energy in the thermally-activated glide rule (Eq. 3) for determining the creep and relaxation behaviour. In order to provide further insight into relative importance of thermally-activated glide and static recovery we use the model to examine the creep and relaxation behaviour of pure copper, in which only forest dislocations provide obstacles to dislocation motion. The understanding gained from

evaluating the response of this microstructurally simpler material provides new insights that can be applied to the modelling of more advanced engineering alloys such as 316H stainless steel.

[Table 1 here]

[Figure 5 here]

4.1 EFFECT OF ACTIVATION ENERGY FOR THERMALLY-ACTIVATED GLIDE ON CREEP AND RELAXATION

The micromechanical mechanisms operating during high-temperature creep deformation under stress- and displacement-controlled histories should be the same. Therefore, a physical creep model should predict both forward creep and relaxation using the same set of physical parameters. Preliminary studies of relaxation of 316H at 500°C and 550°C using parameters from fitting the creep behaviour used in [1] ($\alpha_0 = 1$), however, indicate that the SCM under-predicts relaxation with not enough inelastic strain being generated (see Figure 7). When α_0 is large thermally-activated glide is difficult and the resolved shear stress on a slip plane needs to be of the order of the critically resolved shear stress for there to be any significant inelastic deformation. Decreasing the value of α_0 makes thermally-activated glide easier; thus, in a relaxation experiment, inelastic deformation can occur without significant recovery of the dislocation structure. In practice, the detailed response will be determined by a combination of thermally-activated glide and static recovery. Both these processes also combine to give the constant load/stress creep response. This observation suggests that in order to gain understanding of the physical mechanisms of relaxation, the role of the activation energy for thermally-activated glide needs to be investigated in more detail, as represented by the parameter α_0 in Eq. 4.

To investigate the effect of α_0 , forward creep and relaxation modelling of commercially pure copper at 250°C was conducted. Pure copper (FCC) was selected since only dislocation junctions contribute to the internal resistance, allowing a clearer understanding of the role of the activation energy to be gained. The calibration procedure consisted of selecting a value for α_0 ; the static recovery parameter W_c is then

calibrated to provide an accurate fit to the macroscopic creep curves at a given temperature. Consequently, the same values of α_0 and W_c are used to predict the long-term stress relaxation at the same temperature after loading to different initial stress levels. Studies on copper show that the amount of relaxation of stress over a given timescale increases with decreasing value of α_0 and a good fit (Figure 6) to both creep and relaxation deformation modes is obtained for $\alpha_0 = 0.18$ – a value within the physical range $\alpha_0 = 0.1 \sim 2$, suggested by [55]. All other physical properties and parameters for both Cu are summarised in Table 2.

[Table 2 here]

[Figure 6 here]

The observations on copper suggest that the α_0 and W_c should be determined by simultaneously fitting both creep and relaxation data. The procedure employed for copper was repeated for EX 316H at 500 and 550°C for start of dwell stresses in the range 170-250 MPa. The results are shown in Figures 7 and 8. Again we find that the amount of relaxation increases with decreasing value of α_0 , with a good fit to the relaxation being obtained for $\alpha_0 = 0.18$. It is interesting to note that this value is exactly the same as that obtained for copper (see Figures 7 and 8). An example of forward creep curves obtained via the SCM at 550°C and stress levels of 250 and 280 MPa with $\alpha_0 = 0.18$ are shown in Figure 9; the predictions of constant stress creep are in good agreement with the experimental data. For brevity, other forward creep curves are omitted. It is important to note the significant cast-to-cast variation of creep response of 316H stainless steel, illustrated in Figure 9 by comparing three macroscopic creep curves at 550°C and 250 MPa; variation in deformation response between different casts of this alloy is well-known, e.g. [69]. Hence, we aim to calibrate the model employed in the present study in order to capture the trend and magnitude of existing experimental data for a given cast. The full set of parameters for the 316H material are shown in Table 1. The contribution from the precipitates to the athermal internal resistance was

calculated by considering the experimentally-measured distribution of intragranular $M_{23}C_6$ particles in EX 316H [2]. The solute resistance was estimated by selecting a value of 0.000457 for α_s and considering the concentration of strengthening alloying elements in the material, after [30].

[Figure 7 here]

[Figure 8 here]

The findings confirm the significant effect of α_0 on relaxation, the value found is also consistent with the lower end of the range ($\alpha_0 < 1$) in [55] identified with thermal activation over dislocation junctions. This is consistent with the observation that the major contribution to τ_{cr} is from dislocation junctions and solute complexes, if present, and not precipitates [45]. This also suggests that the value of α_0 for copper and 316H should be approximately equal to each other, which they are. These observations on the activation energy for bypassing and its relation to the types of obstacles in 316H are discussed in more detail in Section 7.

[Figure 9 here]

5. MODELLING CYCLIC DEFORMATION

Cyclic deformation of EX 316H at 550°C under strain-controlled loading was investigated via the enhanced multi-scale SCM considering the mechanisms in Figure 4, together with studies on commercially pure Cu at 250°C. The model for dynamic recovery introduced in Section 3 was applied to each slip plane in the FCC crystal. The calibration procedure of the model consists of predictions of tension-compression cyclic deformation response to saturation of the hysteresis loop for a range of ΔL_r , while all other parameters are the same as those presented in Table 2. The value of L_r in Eq. 10. is selected to be the atomic spacing, a , and Δ is in the range 8~38 (see Table 2). Predictions of both 316H and Cu agree well with experimental data for both symmetric and asymmetric strain-controlled loads

with the introduction of only one additional fitting parameter controlling dynamic recovery. An asymmetric strain range of 0.6% and a symmetric strain range of 1.2% were selected for 316H stainless steel (Figure 10) and commercially pure copper (Figure 12), respectively. Preliminary studies on cyclic deformation of EX 316H at 550°C were also carried without the incorporation of dynamic recovery using only the hardening models from Section 2 and the hardening fitting parameter from Table 2.

[Figure 10 here]

Comparison between predictions using the SCM with and without the model from Section 3 in Figure 11 demonstrates the significance of dynamic recovery with accumulation of cycles. The competition between hardening and dynamic recovery gives rise to a steady state distribution of dislocation link lengths after a number of cycles. This, together with the changing residual stress state during a cycle in the polycrystalline aggregate determines the form of the saturated stress-strain curve. In the absence of dynamic recovery, the material continually hardens and in the cyclic state it is only the changing residual stress state that determines the material cyclic response. The gradual increase of the extent of dynamic recovery is also evident with accumulation of cycles, which is expected since the probability of segment length annihilation increases with increasing dislocation junction obstacle density.

[Figure 11 here]

[Figure 12 here]

Dynamic recovery was tuned to predict saturation for 316H around the 80th cycle [44] and for Cu after the 30th cycle [14] according to experiments. The fact that the model also predicts quite accurately the cycle-to-cycle response up to saturation also gives confidence in the micromechanical model of dynamic recovery employed. In the following section the parameters determined here for cyclic deformation are combined with those determined in Section 4 for creep and relaxation to simulate the material response when a cycle contains “strain dwells”. We also assess the effects of cyclic loading on creep. It should be

noted that the inclusion of dynamic recovery can also affect the creep and relaxation response. Before simulating the behaviour under combined cycles, the full model obtained by combining terms determined from creep/relaxation and cyclic loading tests was used to re-simulate the individual experiments. The results were not altered, which indicates that for the small strain levels considered here, dynamic recovery has a limited effect on the creep and relaxation behaviour for these materials.

6. STRAIN DWELLS DURING CYCLIC LOADING

Parameters established for 316H and copper through fitting the monotonic elastic/plastic, creep-relaxation and cyclic deformation behaviour are used in this section to assess the effects of prior cyclic loading on creep deformation. Four different histories, motivated from a study by Fookes et al. [44], are investigated for both 316H and copper – 1) saturation followed by same strain dwells, 2) maximum strain dwells at each cycle to saturation, 3) zero strain dwell at each cycle to saturation and 4) saturation followed by different strain dwells. It is important to note that the predicted cyclic-relaxation behaviour is independent of any free parameters, all parameters used in the simulations are those determined in the two preceding sections.

6.1 SATURATION AND SAME STRAIN DWELLS (TYPE I HISTORY)

Prior strain-controlled cycling to saturation (80 cycles) was simulated for EX 316H at 550°C with $\varepsilon_{min} = -0.1\%$ and $\varepsilon_{max} = 0.5\%$ at 0.025%/s. Following saturation of the stress-strain curve, another 28 cycles were carried out with 50-hour strain dwells at $\varepsilon_{dwell} = 0.4\%$. The stress-strain response for the 101st-105th cycles is shown in Figure 13. Stress relaxation behaviour was recorded at each cycle (81st to 108th) and compared to experimental data available from [44]. The model predicts the relaxation behaviour well (Figure 14) and also confirms the increase in extent of stress relaxation with cycles, as observed in [44]. This behaviour was also noted in predictions on copper, but results on copper are omitted here for brevity.

[Figure 13 here]

[Figure 14 here]

6.2 MAXIMUM STRAIN DWELLS TO SATURATION (TYPE 2 HISTORY)

Three prior sub-histories in three different samples – a) maximum strain dwell at each cycle to saturation at σ_{max} , b) primary and secondary creep at σ_{max} and c) monotonically increasing load to σ_{max} at rate of 0.025%/s - of 316H at 550°C were simulated and subsequent long-term relaxation behaviour was compared across the three types of test (Figure 15). Relaxation for a type a) history in which the material experienced strain dwells of 50 hours for 80 cycles in which the total strain was cycled between -0.4% and 0.4% , which resulted in a saturated cycle with a maximum stress of $\sigma_{max} = 285$ MPa is compared with a type b) relaxation test following creep at 285 MPa (489 hours, 550°C) and a type c) relaxation test following monotonic loading to the same stress level. The saturated type a) cycle is shown in Figure 16.

[Figure 15 here]

Predictions of the relaxation behaviour are given in Figure 17 and show that most stress relaxation is achieved after monotonic loading. Creep into the secondary regime produces the least amount of relaxed stress. An interesting finding is that the cyclic-dwell history results in a stress drop behaviour in between prior monotonic loading and creep (Figure 17). The three relaxation curves also appear to be converging at large times. Another important observation is that the relaxation after just one cycle is greater than that after the full 80-cycle run. Results for Cu are consistent with observations for 316H.

[Figure 16 here]

[Figure 17 here]

6.3 DWELLS AT ZERO STRAIN TO SATURATION (TYPE 3 HISTORY)

The Type 3 history is similar to the one examined in the preceding section with the major difference being that strain dwells are carried out at $\varepsilon = 0.0\%$ and the maximum saturated stress is selected as $\sigma_{\varepsilon=0\%}$. The effects of strain dwells of 50 hours for 80 cycles between -0.4% and 0.4% strain leading to a saturated $\sigma_{\varepsilon=0\%} = 199$ MPa and creep at 199 MPa (2000 hours, 550°C) on relaxation were assessed again and compared to simple HT relaxation tests in Figure 18. Similar observations on subsequent relaxation behaviour are made to those for a Type 2 loading history. The least stress relaxation results after creep into the secondary regime and the greatest stress drop is experienced after elastic-plastic monotonic loading. The cyclic-dwell history response is in between the two responses with the three curves having a tendency to converge at large times (Figure 19). This would suggest that at longer times recovery during relaxation becomes significant and equilibrates the internal state of the three different histories. Contrary to the Type 2 history, less stress relaxation is observed after the 80th cycle (Figure 20). This observation suggests that the initial stress and strain level have a strong effect on the initial transient [25] which could be linked to the fact that different grain families in the material experience different stresses states, with the distribution of residual stress depending on the history of loading prior to conducting the relaxation test. During relaxation the state of the material evolves and the residual stresses redistribute. Since each type of relaxation tests starts from a different internal residual stress state, the way in which the stress subsequently redistributes and how this influences the evolution of state in each grain plays an important role in determining how the stress relaxes.

[Figure 18 here]

[Figure 19 here]

[Figure 20 here]

6.4 SATURATION AND DIFFERENT STRAIN DWELLS (TYPE 4 HISTORY)

Similar to Section 6.1, prior saturation of 80 tension-compression cycles was carried out on 316H at 550°C. Following saturation, 30 more cycles were carried out with 50-hour strain dwells with the strain-controlled dwell starting at different instants in the cycle, increasing by 0.1% strain from one cycle to the next up to the peak strain level (with the pattern repeating every 5 cycles from the 81st to the 110th cycle). The stress-strain response for the 101st-105th cycles is shown in Figure 21 and compared to experimentally-observed behaviour of the alloy after completion of 136 cycles with smaller strain intervals (0.05%).

[Figure 21 here]

Observations from Figure 21 suggest that the behaviour during subsequent post-dwell re-load is not explicitly captured by the SCM. The experimental data shows a more abrupt change on re-load combined with an increase in the hardening behaviour with cycles. A possible explanation for this is that during a dwell solute atoms can segregate to the dislocations and on reloading a higher stress is required to break the dislocations away from their solute atmosphere. This possibility is not fully included in the current model. Further investigations of the response during the dwell and the subsequent re-load behaviour is required to assess with confidence the cyclic behaviour for this type of loading using the SCM. This is addressed further in Section 7. As for the variation of the relaxation dwell behaviour with cycles, it is found that the extent of relaxation is more dependent on the strain level and initial stress as compared to changes in relaxation with cycles (see Figure 22); the relaxation response here is presented in terms of stress drop magnitude with time since the stress levels at the start of the relaxation dwells at cycles 105, 107 and 108 were different.

[Figure 22 here]

6.5 EFFECTS OF STRAIN RANGE AND RE-INITIATION OF PRIMARY CREEP

The phenomenon of re-initiation of primary creep after load removal or other changes in the loading history is still not well understood. The effect of prior cyclic loading on long-term creep deformation is of importance since life assessment procedures such as R5 are based on the accumulation of creep strain. Experiments have shown that depending on the strain range of the prior cyclic loading history, different creep responses are to be expected [13] in 316H. In order to investigate this phenomenon, we replicate the three loading sub-histories considered in Section 6.2 (Type 2 History) using the SCM crystal plasticity framework with three different strain ranges for the cyclic loading with dwells, namely 0.8%, 0.6% and 0.4%. Instead of attempting to predict forward creep, we focus on the long-term displacement-controlled deformation and its dependence on strain range of the prior cyclic loading. The reason for using lower strain ranges ($\geq 0.4\%$) than the initially-considered ($\Delta\varepsilon = 0.8\%$) is because the former are closer to plant operating conditions, whereas the latter is commonly employed in laboratory experiments. Following the same modelling procedure used in Section 6.2, the saturated σ_{max} after dwells at the maximum strain levels for each strain range considered and the creep loading times are summarized in Table 3.

[Table 3 here]

Comparison between the three sub-history long-term relaxation responses is shown in Figure 23 for each of the three different strain ranges. The overall trends of the three sub-history responses for each strain range are consistent with the observations in Section 6.2. Creep into the secondary regime produces the least amount of relaxed stress upon subsequent relaxation. Predictions of the subsequent relaxation behaviour show that most stress relaxation is achieved after monotonic loading with the three curves having a tendency to converge at longer times. It is important to note that the SCM captures the faster saturation of the cyclic stress-strain curve at lower strain ranges, which has been observed experimentally [13]. The predictions indicate that as the strain range decreases the phenomenon of re-initiation of

primary creep attenuates; the 0.4% strain range cyclic loading history with dwells does not show any “re-priming”. Comparison between the long-term stress drop during relaxation after 0.8% and 0.4% strain ranges is made in Figure 24.

[Figure 23 here]

From a physical perspective, primary creep is dependent on the evolution of the internal state – hardening and static and dynamic recovery due to refinement and coarsening of the dislocation junction network, respectively – and the redistribution of residual stresses between the anisotropic grains. The observations made on the re-initiation of primary creep in this section indicate that cyclic loading at lower strain ranges does not potentially induce such large changes in the residual stress field of the polycrystalline aggregate and the accumulated obstacle density. This is also a possible explanation for the faster saturation of the stress-strain curve at lower strain ranges.

[Figure 24 here]

Series of different cyclic-dwell loading histories are examined in Section 6 in order to assess the effects of prior cyclic loading on displacement-controlled creep deformation. SCM results of relaxation behaviour during strain dwells, presented in Section 6.1, indicate that the model predictions agree well with the trends in macroscopic deformation response observed in the experimental data available. Comparison between predictions in Sections 6.2, 6.3 and 6.5 suggest that the model employed in this study captures the expected trends in creep response as a result of prior loading histories, suggested in [13,44], although experimental data for direct comparison is not available. Further considerations on the physics behind the dislocation interactions with solute atmospheres at high temperatures should be made in order for the model employed to predict more accurately the stress-strain response behaviour upon subsequent re-load after the strain dwell, as demonstrated in Section 6.4. Effects of both evolution of internal state and redistribution of residual stress fields are found to control the deformation behaviour,

providing a physical basis for the “back stress” employed in other studies. Further understanding is gained of the effects of prior loading on subsequent creep strain accumulation, however, improvements need be made in the predictions of post-dwell re-load as this detailed deformation process is not yet fully understood.

7. PRIOR PLASTICITY EFFECTS ON CONSTANT STRESS CREEP DWELL

In this section the effects of the evolution of microstructural state and residual stress field during cyclic loading on the response during constant stress creep dwells is examined. In addition to the effects of cyclic plasticity on constant strain dwells (Section 6), its effect on forward constant stress creep is also of importance to plant operation since constant primary stresses can also arise during service [70]. The SCM framework and microstructural model employed in the present study can potentially inform empirical models used in industry to capture better the creep strain accumulation during complex loading histories; therefore, the aim here is to broaden the scope of the predictive capabilities of the developed SCM in terms of capturing the cyclic-creep interactions in Type 316H stainless steel. This will provide greater confidence in the developments of the micromechanical model as part of this study with regard to the evolution of the dislocation network during cyclic loading, resulting from the balance between self/latent hardening and dynamic recovery. Predictions via the SCM of creep strain accumulation during hold-stress dwells at high temperature, introduced at different cycles, are compared against existing experimental data and used to explain the effect of prior cyclic hardening on subsequent creep response. The importance of the Type II (intragranular) residual stress field in the polycrystalline aggregate resulting from prior cyclic loading will be assessed by introducing tensile creep dwells after which re-loading to the desired stress is carried out from the point where the cyclic stress state cuts the zero-stress axis during either the tensile or compressive part of the cycle.

7.1 MODEL CALIBRATION

A recent study by Mamun [67] evaluated experimentally the changes in high temperature creep response of solution-treated 316H austenitic stainless steel, whose composition is shown in Table 4, as a result of different prior cyclic histories. The cyclic tension-compression loading was strain-controlled in the range $\pm 1\%$. Creep tests at the same stress level of 120 MPa and at a temperature of 650°C were carried out on three different specimens (A-C) with varying cyclic histories, as described in [67]. Specimen A) was monotonically loaded to +1.0% strain in tension; Specimen B) was unloaded after the second loading cycle and re-loaded to the same stress reached for Specimen A; and Specimen C) was re-loaded to the same applied stress of Specimen A and B from a compressive peak strain of -1.0% in the third loading cycle. The SCM was first calibrated to replicate the monotonic elastic-plastic and cyclic stress-strain response of the alloy at 650°C (Figure 25) by adjusting the parameters controlling the initial obstacle density, self/latent hardening and dynamic recovery (see Table 5). Constant stress creep dwells in tension with a duration of 15 hours were introduced after the respective cyclic history for each sample (Figure 26). Following the calibration of monotonic/cyclic deformation behaviour, the static recovery controlling parameter W_c was calibrated to predict correctly the creep response at the desired temperature upon monotonic load-up in tension (Type A History, Figure 27). The previous sections demonstrated that an appropriate value for α_0 is 0.18. Contribution from the precipitates to the internal resistance was ignored as solution-treated material is being examined. It should be noted that phase transformations are not included in the model here under the assumption that the creep test periods are too short for any significant precipitate phases to form [30,71]. The solute resistance was estimated by selecting the same value of 0.000457 for α_s and considering the concentration of strengthening alloying elements (Table 4) in the material. All other physical properties and parameters for Type 316H stainless steel are summarised in Table 5. Predictions of the creep response for each of the three samples, which are independent of free parameters, are shown in the following subsection.

[Table 4 here]

[Table 5 here]

[Figure 25 here]

[Figure 26 here]

7.2 THE ROLE OF CYCLIC HARDENING AND RESIDUAL STRESS STATE

Model predictions of the creep response during constant stress dwells for each of the three Specimens A-C are presented in Figure 27 and compared against the experimental data obtained by Mamun [67]. The SCM predictions capture well the trend in experimental results; the largest amount of creep strain is accumulated during the dwell in Specimen A and the least amount – in Specimen B with the creep response of Specimen C in between. Both Specimens B and C demonstrate lower amounts of creep strain accumulated during primary creep compared to Specimen A, agreeing with observations made in [41,42,67,72]. Although the model prediction overestimates the accumulation of creep strain with time for the Type A history, the difference with experimental data is by approximately a factor of two which is acceptable based on the observations of scatter in deformation response of Type 316 stainless steel across different and similar casts [69]. The simulation results further confirm the effect of reduction in the extent of the primary creep stage for pre-strained austenitic stainless steel. The phenomenon is believed to be the result of the evolution of the dislocation network in the material, as described by Ajaja and Ardell [43] for AISI Type 304 and Joseph et al. [13] for AISI Type 316 austenitic stainless steels. During cyclic loading the dislocation structure is refined due to the reduction in spacing between the obstacles to dislocation motion, resulting from the intersection between dislocation link segments during slip [2], as part of the continuous interaction between self/latent hardening and dynamic recovery. Once the dislocation obstacle network is refined, a balance between hardening and thermal (static) recovery at high temperature during creep loading is reached faster since the rate of static recovery by dislocation

climb processes would be greater for the higher dislocation densities, as suggested by Morris and Harris [28]. The reduction of creep rate during primary creep is believed to be as a result of the competition between hardening and static recovery until a dynamic balance between the two processes is reached, which is taken as the start of the secondary creep stage, where the creep rate usually reaches a minimum [1]. This confirms the explanation of the reduction in primary creep strain accumulation after pre-straining as a result of refinement of the dislocation forest network during cyclic hardening.

The redistribution of stress between grains during inelastic deformation of polycrystalline materials is another phenomenon which is observed to control the accumulation of inelastic strain during the primary creep stage, as noted by Hu and Cocks [1]. Similar observations were also made in Section 6 of the present study with regards to the transient stage of stress relaxation at high temperatures. It is clear from Figure 27 that, compared to Specimen C, the primary creep stage is not evident for Specimen B, which was unloaded from a tensile macroscopic state of stress and re-loaded in tension to 120 MPa, where the dwell began. Mamun [67] suggests that the difference in primary creep between Specimens B and C is due to the unloading in Specimen B which reverses the dislocation motion direction resulting in a lower number of mobile dislocations necessary for primary creep. This explanation is questionable since 1) not a significant amount of hardening would be expected during the unloading from such moderate levels of stress and 2) similarities in hardening rates and dislocation structures in the two samples are shown in [67]. In addition, modelling results on the resultant dislocation obstacle spacing from this study show minor differences between the two specimens prior to creep loading. The resultant Type II (intragranular) residual stress fields in Specimens B and C are however different. The lack of a primary creep stage during the tensile dwell in Specimen B can be explained through the existence of an intragranular residual stress field generated at the peak tensile strain position, which allows for compatible plastic deformation during the subsequent tensile dwell. This explanation agrees with the observations made by Hu et al. [45] and Hu and Cocks [1] with respect to the stress redistribution between the grains as a requirement for the

establishment of a suitable stress field for compatible inelastic deformation during monotonic elastic-plastic and forward creep deformation histories.

[Figure 27 here]

The minimum creep strain rates predicted by the SCM agree with the experimental data, although the steady-state response predicted for Specimen B is significantly lower (Figure 28). Specimen A experiences the fastest creep rate while the creep rate of Specimen C is slightly lower. The reason behind this is the hardened state of Specimen C as a result of prior cyclic history, agreeing with Joseph et al. [13]; dislocation motion in Specimen C would be more difficult due to the higher dislocation obstacle density and thus, once an equilibrium is reached between hardening and static recovery, the strain rate would be lower [41]. The lowest steady-state strain rate is both recorded experimentally and predicted via the SCM for Specimen B. The presence of a more pronounced primary creep stage in Specimen C, however, will result in redistribution of stress between the grains, causing some grains to deform at higher rates than others. Differences in the microstructural evolution during the primary creep stage would potentially cause differences in the equilibrium state of the dislocation network during steady-state creep in the two specimens, which agrees with both modelling results on the average dislocation obstacle spacing (not shown here for brevity). These observations further confirm the explanation of the primary creep stage being the result of the stress redistribution processes between individual grains and the interaction between hardening and thermal recovery of the dislocation structure at high temperature and prolonged loading periods. Based on this explanation, different equilibria between the stress redistribution and hardening-recovery interactions would result in different dislocation obstacle structures and, hence, different minimum creep rates (under the assumption that residual stresses do not evolve during the secondary creep stage in materials where no phase transformation are expected during long-term high-temperature exposure, e.g. ex-service 316H [33]).

[Figure 28 here]

8. DISCUSSION

Enhancement of the existing multi-scale self-consistent model to be able to more fully model cyclic deformation and predict accurately relaxation from forward creep introduces another two free parameters to the three parameters identified by Hu and Cocks [2], describing the initial yield strength, hardening and static recovery. Hence, by only using five fitting parameters representing: i) the initial dislocation structure; ii) self/latent hardening; iii) static recovery; iv) dynamic recovery and v) activation energy for thermally-activated glide, the developed model is able to predict four different loading conditions, namely elastic-plastic, forward creep, cyclic and relaxation deformation. It is important to note that each of the free parameters are motivated from the essential physics of the different processes considered, hence allowing a clearer understating of physical phenomena behind deformation to be gained.

Predictions of relaxation behaviour using parameters obtained from fitting the model to forward creep curves shows that the accumulation of creep strain as a physical process is the same under stress- and displacement-controlled high temperature loading at prolonged times. Model predictions agree well with experimental data. Moreover, the SCM provides a possible physical explanation of the widely-used “back stress” term and observations made in this study can be used to help choose its magnitude in more simplistic models. The global response is dependent on a combination of the evolution of the internal state, represented by the changes in the network of obstacles to dislocation motion, and the redistribution of residual stresses between the grains. The significance of the physical phenomenon of dislocations bypassing sets of obstacles, described by the mechanistic thermally-activated glide flow rule, is established in this study. The parameter α_0 which controls the activation energy for bypassing, hence the overall effectiveness of obstacles, is found to control the deformation response. Frost and Ashby [55] provide guidelines in the setting of α_0 through mechanistic considerations - $2 > \alpha_0 > 1$ for strong

obstacles (precipitates), $\alpha_0 < 1$ for medium obstacles (dislocation junctions) and $\alpha_0 \ll 0.2$ for weak obstacles (solute atoms). The parameter α_0 is treated as a physical constant, which can be tuned depending on the material examined. In a previous study by Hu and Cocks [29] focusing on monotonic and forward creep loading using the SCM from Section 2, with α_0 set to unity, under the assumption that the averaged contribution of the three major obstacles in 316H would result in the mean of the whole range given in [55]. All other parameter controlling hardening and softening are determined once α_0 is selected. The present study demonstrates that accurate predictions of both forward creep and relaxation behaviour is obtained when α_0 is at the mid-to-lower end of the physical range identified in [55]. This indicates that the major contribution to obstacles to dislocation motion are dislocation junctions, together with a moderate contribution of solute atoms. Hence, a lower value of the activation energy allows generation of creep strain over a wider range of $\tau^{(\alpha)}/\tau_{cr}^{(\alpha)}$ ratios at the temperatures considered here. Initial relaxation transients and the subsequent steady-state regimes are captured better with the thermal activation parameter employed here.

The self-consistent modelling framework employed in the present study possesses certain limitations which could lead to inaccuracies in the modelling predictions. The SCM is formulated within small deformation theory where texture evolution is not captured, as lattice rotations are ignored. Large deformation theory, on the other hand, captures such lattice rotations with respect to a reference co-ordinate system resulting in the re-orientation of the crystal with respect to the loading axis. The evolution of texture provides further hardening or softening effects locally which potentially influence the global deformation response of the alloy. It is expected that texture effects will be more pronounced at larger strains accumulated, however, the small-deformation SCM employed here was compared to a large-deformation crystal plasticity finite element (CPFE) model in [10], employing the same constitutive models, showing good agreement between the two modelling approaches under global strains of 10%. Another limitation of the SCM model here, which employs an explicit numerical scheme, is the potential

time step sensitivity. With regards to the micromechanical models embedded within the present SCM framework, a limitation in its predictive capabilities arises in the very long-term and low-stress creep regime where dislocation climb activity over intragranular second-phase particles may become important [11]. The coupling between dislocation glide and climb over obstacles in the present model is a current requirement as under plant operating conditions at lower stresses dislocation climb mechanisms could potentially be the dominant deformation process in Type 316 stainless steel.

Cyclic deformation is captured well by the SCM through the incorporation of the simplistic physical model of dynamic recovery, introduced in Section 3. The model is able to capture the change in internal state of the material during deformation and the evolution of the internal residual stress fields (microscopic and intragranular), both of which are observed to influence the macroscopic response of the polycrystalline aggregate. The extent of dynamic recovery increases with accumulation of inelastic strain which affects the local stress state and global response. It is important to note that in this study no dislocation cell formation within the grains was assumed, since at the temperature range of interest and no cell structures have been observed experimentally [62]. At higher temperatures ($>700^{\circ}\text{C}$) dislocation cells or subgrains may form and the dynamic recovery model employed in this study may not produce accurate predictions, since the distribution of dislocation segments will not be uniform, but concentrated at the cell walls.

Predictions of cyclic deformation with strain dwells are able to provide further understanding of possible effects of cyclic load on subsequent accumulation of creep strain; we hypothesise that such insights could potentially be used by industry to enrich the phenomenological frameworks employed to predict creep strain accumulation and damage development during plant cycles. In a future article we demonstrate how the modelling approaches presented here could be employed in a more systematic way to predict deformation scenarios replicating those under plant operation and provide guidelines for improvement of the existing models in the R5 and R66 structural assessment procedures in the UK.

Modelling of such combined deformation histories, i.e. cyclic loading and relaxation, was carried out independently of any free parameters – those used were established through separate modelling and fitting to experimental data of each independent deformation mode. The experimentally-observed increase in extent of stress relaxation with cycles with dwells at the same strain level is confirmed by the SCM predictions for 316H and copper. However, model predictions of relaxation dwells at different strain levels during cyclic loading show that relaxation at larger constant strain and larger initial stress levels result in greater stress drop during the initial transient stages of the dwell since higher initial stress will be associated with higher magnitude of the residual intragranular stresses.

The effects of prior cyclic loading with strain dwells and prior creep deformation into the secondary regime on long-term relaxation were assessed through a series of loading histories. Model predictions show that prior cyclic and monotonic creep deformation harden the polycrystalline structure which results in less relaxation, as compared to relaxation after monotonic elastic-plastic loading. At longer times (>800 h), however, the thermal recovery of the microstructure becomes dominant and the dislocation obstacle network equilibrates. This causes the residual stress field to redistribute resulting in convergence of the three global relaxation responses across the sub-histories considered. Comparison between the long-term relaxation response after cyclic loading with dwells at maximum and zero strain level to saturation further confirms the dominance of the initial stress in determining the response during the initial transient stage [25,73].

The effects of prior plasticity on subsequent forward creep dwells have been examined in Section 7. The extent of creep strain accumulation during primary creep was found to decrease after prior straining of the material, agreeing with [41–43,72], as a result of the cyclic hardening and changes in the residual stress field. The strain range of 2% examined in this study is, however, more relevant to laboratory testing and not as much to power plant operating conditions. Therefore, the effect of prior cyclic plasticity at shorter strain ranges on forward creep should be examined in more detail. Model predictions show that

the steady-state creep rate was also found to decrease as a result of prior plasticity, agreeing with Joseph et al. [13]. Studies in the literature [43] show that the effect of prior cyclic loading on reduction of the secondary creep rate diminishes for higher values of creep hold stress (with respect to the saturated cyclic stress amplitude). A possible reason for this would be the more pronounced effect of thermal recovery at higher stresses transforming the dislocation structure established during cyclic hardening prior to creep. Transient effects at longer creep times will possibly diminish and thermal recovery will equilibrate the dislocation network, which could lead to similarities in the resulting steady-state creep rates for monotonic load-up creep tests and those with a significant amount of pre-straining, as observed by [41]. The effects of thermal recovery during prolonged creep tests on ex-service 316H will be examined in a future study by the authors. It is also important to note that the simulations carried out in Section 7 are compared against creep test data over relatively short times. For this solution-treated austenitic stainless steel at longer times, however, the additional effects of phase transformations on internal resistance and Type III microscopic residual stress will play an important role [29].

Modelling the Type 3 history introduced in Section 6.3 motivated the assessment of cyclic loading strain range effects on subsequent creep response with emphasis on the re-initiation of primary creep. Examination of the three different ranges (0.4% ~ 0.8%) indicated that at 0.4% and below no such “re-priming” phenomenon was evident during long-term stress relaxation at 550°C. This is attributed to the fact that at lower strain ranges the changes in the internal state and evolution of residual stress fields are minor. Hence, the effect of lower strain ranges during prior cyclic loading on subsequent long-term creep is insignificant and primary creep does not fully re-appear. The importance of this finding is related to the potential modifications of existing assessment procedures for creep strain accumulation estimation – lower strain ranges ($\approx 0.4\%$) are closer to plant operating conditions, whereas strain ranges of the order 0.8% are commonly employed in laboratory experiments. The SCM relaxation studies can provide further insight into how parameters in simplistic models for creep deformation used by industry should

be established, as well as providing an understanding of the underlying physics of deformation process during relaxation and how this relates to forward creep.

9. CONCLUSIONS

- I. Enhancements of the existing SCM in predicting relaxation from forward creep and cyclic loading requires another two free parameters in the multi-scale model developed by Hu and Cocks [2]. With these enhancements, the SCM is able to predict four deformation modes – monotonic elastic-plastic, creep, relaxation and cyclic loading – using only five fitting parameters.
- II. The activation energy for thermally-activated glide has a significant effect on stress relaxation. The parameter α_0 , which controls the overall effectiveness of obstacles, was found to be 0.18 for both 316H stainless steel and copper. This value gives accurate predictions for both forward creep and relaxation. This is consistent with the major contribution to internal resistance being from dislocation junctions.
- III. Incorporation of dynamic recovery in the model allows the accurate prediction of the macroscopic stress-strain response during cyclic loading. The deformation behaviour is controlled by the changes in the internal state and evolution of the internal residual stress field.
- IV. Model predictions for cyclic loading with strain dwells of a given duration show an increase in extent of relaxation with increasing cycles. Predictions of cyclic loading with different strain dwells, however, indicate that relaxation is mainly dependent on the initial stress and level of constant strain.
- V. Predictions of history-dependent long-term relaxation show that the least stress relaxation results after creep into the secondary regime and the greatest stress drop is experienced after simple high temperature elastic-plastic monotonic loading. The cyclic-dwell history response is in between these two responses, with the three relaxation curves having a tendency to converge at large times.

- VI. The extent of primary and secondary creep stages during constant stress dwells decreases following prior cycling. Prior cycling, during which a suitable stress field for compatible plastic deformation is established, results in a near-complete removal of the primary creep regime upon subsequent loading to a constant stress level.
- VII. Re-initiation of primary creep after a prior cyclic-dwell loading history is dependent on the strain range. At a strain range of 0.4% and below, predictions via the SCM indicate that “re-priming” of primary creep is insignificant.

10. ACKNOWLEDGEMENTS

The authors are grateful to EDF Energy plc for supplying the experimental data and supporting the research described in this paper. M.P.P would like to thank Marc Chevalier and Mike Spindler at EDF Energy plc for useful discussions.

REFERENCES

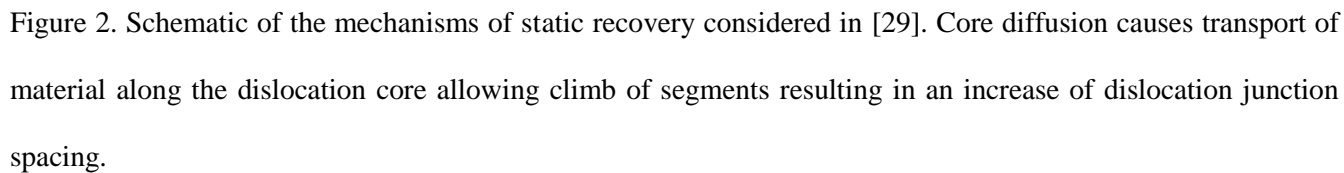
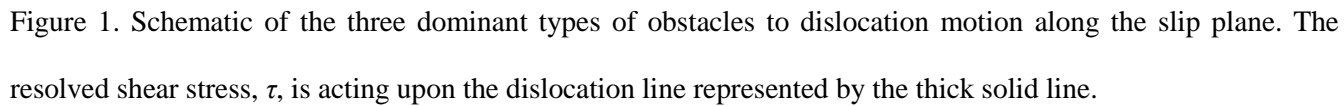
- [1]. Hu JN, Cocks ACF. Effect of creep on the Bauschinger effect in a polycrystalline austenitic stainless steel. *Scr. Mater.* 2017;128:100–4.
- [2]. Hu J, Cocks ACF. A multi-scale self-consistent model describing the lattice deformation in austenitic stainless steels. *Int. J. Solids Struct.* Elsevier Ltd; 2016;78–79:21–37.
- [3]. Oka Y, editor. Nuclear Reactor Design. Springer BV; 2010.
- [4]. Spindler MW. Observations regarding creep in 316H (EDF Energy), HT Forum. 2011.
- [5]. Chen B, Smith DJ, Flewitt PEJ, Spindler MW. Constitutive equations that describe creep stress relaxation for 316H stainless steel at 550 deg C. *Mater. High Temp.* 2011;28:155–64.
- [6]. Cui Y, Sauzay M, Caes C, Bonnaillie P, Arnal B, Cabet C, Blat-Yrieix M, Dubiez-Legoff S. Modeling and experimental study of long term creep damage in austenitic stainless steels. *Eng. Fail. Anal.* Elsevier Inc.; 2015;58:452–64.
- [7]. Wen J-F, Tu S-T, Xuan F-Z, Zhang X-W, Gao X-L. Effects of Stress Level and Stress State on Creep Ductility: Evaluation of Different Models. *J. Mater. Sci. Technol.* Elsevier Ltd; 2016;32:695–704.
- [8]. Kocks UF, Mecking H. Physics and phenomenology of strain hardening: The FCC case. *Prog. Mater. Sci.* 2003;48:171–273.

- [9]. Hyde CJ, Sun W, Leen SB. Cyclic thermo-mechanical material modelling and testing of 316 stainless steel. *Int. J. Press. Vessel. Pip.* Elsevier Ltd; 2010;87:365–72.
- [10]. Chaboche JL, Rousselier G. On the Plastic and Viscoplastic Constitutive Equations - Part I: Rules developed with internal variable concept. *J Press Vessel Technol.* 1983;150:153–8.
- [11]. Chaboche JL, Rousselier G. On the Plastic and Viscoplastic Constitutive Equations - Part II : Application of internal variable concepts to the 316 Stainless steel. *J Press Vessel Technol.* 1983;105:159–64.
- [12]. Gong YP, Hyde CJ, Sun W, Hyde TH. Determination of material properties in the Chaboche unified viscoplasticity model. *Proc. Inst. Mech. Eng. Part L J. Mater. Des. Appl.* 2010;224:19–29.
- [13]. Joseph TD, McLennon D, Spindler MW, Truman CE, Smith DJ. The effect of prior cyclic loading variables on the creep behaviour of ex-service type 316H stainless steel. *Mater. High Temp.* 2013;30:156–60.
- [14]. Dunne FPE, Hayhurst DR. Continuum damage based constitutive equations for copper under high temperature creep and cyclic plasticity. *Proc.R.Soc.Lond.A.* 1992;437:545–66.
- [15]. Bruzzi MS, McHugh PE, O'Rourke F, Linder T. Micromechanical modelling of the static and cyclic loading of an Al 2124-SiC MMC. *Int. J. Plast.* 2001;17:565–99.
- [16]. Turkmen HS, Dawson PR, Miller MP. The evolution of crystalline stresses of a polycrystalline metal during cyclic loading. *Int. J. Plast.* 2002;18:941–69.
- [17]. Wang Y. Design, Development and Experiments to Investigate the Effect of Elastic Follow-up on Creep Stress Relaxation in Austenitic Steels. University of Bristol; 2015.
- [18]. Coleman SL. Stress Relaxation of Ex-Heysham 1 Superheater Header Type 316H Stainless Steel. 1996.
- [19]. Wang H, Clausen B, Tomé CN, Wu PD. Studying the effect of stress relaxation and creep on lattice strain evolution of stainless steel under tension. *Acta Mater.* 2013;61:1179–88.
- [20]. Martin U, Mühle U, Oettel H. Stress Relaxation in Superalloys Due to Microstructural Changes. *Mech. Time-Dependent Mater.* 1998;2:1–12.
- [21]. Wang YQ, Spindler MW, Truman CE, Smith DJ. Critical analysis of the prediction of stress relaxation from forward creep of Type 316H austenitic stainless steel. *Mater. Des.* Elsevier Ltd; 2016;95:656–68.
- [22]. Cocks ACF. Final report on constitutive modelling and stress relaxation of 316 stainless steel. 1996.
- [23]. Feltham P. Creep and stress relaxation in alpha-brass at low temperatures. *Philos. Mag.* 1961;6:259–70.
- [24]. Rohde RW, Swearingen JC. Metal deformation modelling – stress relaxation of aluminium. *ASTM STP 676.* 1979. p. 21–34.
- [25]. Hart EW, Solomon HD. Load relaxation studies of polycrystalline high purity aluminium. *Acta Mater.* 1973;21:295–307.

- [26]. Hormozi R, Biglari F, Nikbin KM. Experimental study of Type 316 stainless steel failure under LCF/TMF loading conditions. *Int. J. Fatigue*. 2015;75:153–69.
- [27]. Morris DG. Creep in Type 316 Stainless steel. *Acta Metall*. 1978;26:1143–51.
- [28]. Morris DG, Harries DR. Recovery of a creep-deformed Type 316 stainless steel. *J. Mater. Sci*. 1979;14:2625–36.
- [29]. Hu J, Cocks ACF. Correlation Between Microstructure Evolution and Creep Properties of Polycrystalline Austenitic Stainless Steel. *Trans. SMiRT-23 Manchester, United Kingdom*. 2015.
- [30]. Hu J. A theoretical study of creep deformation mechanisms of Type 316H stainless steel at high temperature. DPhil Thesis, University of Oxford; 2015.
- [31]. Morris DG, Harries DR. Creep and rupture in Type 316 stainless steel at temperatures between 525 and 900°C Part II: Rupture and ductility. *Met. Sci*. 1978;12:532–41.
- [32]. Chen B, Hu JN, Flewitt PEJ, Smith DJ, Cocks ACF, Zhang SY. Quantifying internal stress and internal resistance associated with thermal ageing and creep in a polycrystalline material. *Acta Mater*. 2014;67:207–19.
- [33]. Chen B, Hu JN, Wang YQ, Kabra S, Cocks ACF, Smith DJ, Flewitt PEJ. Internal strains between grains during creep deformation of an austenitic stainless steel. *J. Mater. Sci*. 2015;50.
- [34]. Miller AK. An inelastic constitutive model for monotonic, cyclic and creep deformation: Part I - Equations development and analytical procedures. *J Eng Mater-T*. 1976;96:97–105.
- [35]. Roters F, Eisenlohr P, Hantcherli L, Tjahjanto DD, Bieler TR, Raabe D. Overview of constitutive laws, kinematics, homogenization and multiscale methods in crystal plasticity finite-element modeling: Theory, experiments, applications. *Acta Mater*. 2010;58:1152–211.
- [36]. Mecking H, Kocks UF. A Mechanism for Static and Dynamic Recovery [Internet]. *Strength Met. Alloy*. Pergamon Press Ltd; 1979.
- [37]. Kocks UF. Laws for Work-Hardening and and Low-Temperature Creep. *J. Eng. Mater. Technol*. 1976;76–86.
- [38]. Estrin Y, Kubin LP. Local strain hardening and nonuniformity of plastic deformation. *Acta Metall*. 1986;34:2455–64.
- [39]. Wang H, Wu PD, Tomé CN, Huang Y. A finite strain elastic-viscoplastic self-consistent model for polycrystalline materials. *J. Mech. Phys. Solids*. 2010;58:594–612.
- [40]. Dunne FPE, Rugg D, Walker A. Lengthscale-dependent, elastically anisotropic, physically-based hcp crystal plasticity: Application to cold-dwell fatigue in Ti alloys. *Int. J. Plast*. 2007;23:1061–83.
- [41]. Fookes A, Li SX, Smith DJ. Influence of prior cyclic hardening on high temperature deformation and crack growth in Type 316L(N) stainless steel. *Mater. High Temp*. 1999;15:187–93.
- [42]. Kikuchi S, Ilschner B. Effects of a small prestrain at high temperature on the creep behaviour of AISI 304 stainless steel. *Scr. Mater*. 1986;20:159–62.

- [43]. Ajaja O, Ardell AJ. The effect of prior cold work on the creep characteristics of AISI Type 304 austenitic stainless steel. 1978.
- [44]. Fookes A, Li S, Smith DJ, Spindler M. Stress relaxation during dwells for creep and fatigue cycling of Type 316H stainless steel at 550 deg C. *2nd Int. ECCC Conf. Creep Fract. High Temp. Components-Design Life Assessment*. 2009;1–10.
- [45]. Hu J, Chen B, Smith DJ, Flewitt PEJ, Cocks ACF. On the evaluation of the Bauschinger effect in an austenitic stainless steel—The role of multi-scale residual stresses. *Int. J. Plast.* Elsevier Ltd; 2016;84:203–23.
- [46]. Hu J, Chen B, Smith DJ, Flewitt PEJ, Cocks ACF. Self-consistent Modelling and the Evaluation of Lattice Deformation in a Polycrystalline Austenitic Stainless Steel. *Mater. Today Proc.* 2S. Elsevier Ltd.; 2015. p. S424–33.
- [47]. Petkov M, Hu J, Tarleton E, Cocks ACF. Comparison of self-consistent and crystal plasticity FE approaches for modelling the high-temperature deformation of 316H austenitic stainless steel. *Int. J. Solids Struct.* 2018;to appear.
- [48]. Hull D, Bacon DJ. Introduction to Dislocations. 5th ed. Elsevier; 2011.
- [49]. Asaro RJ, Needleman A. Texture development and strain hardening in rate dependent polycrystals. *Acta Metall.* 1985;33:923–53.
- [50]. Asaro RJ. Micromechanics of Crystals and Polycrystals. Adv. Appl. Mech. 1983.
- [51]. Schmid E, Boas W. Plasticity of crystals: with special reference to metals. Springer US; 1968.
- [52]. Kocks UF, Argon AS, Ashby MF. Thermodynamics and Kinetics of Slip. *Prog. Mater. Sci.* 1975;19:1–291.
- [53]. Schmidt CG, Miller AK. A Unified Phenomenological Model for Non-Elastic Deformation of Type-316 Stainless-Steel .1. Development of the Model and Calculation of the Material Constants. *Res Mech.* 1981;3:109–29.
- [54]. Schmidt CG, Miller AK. A Unified Phenomenological Model for Non-Elastic Deformation of Type-316 Stainless-Steel .2. Fitting and Predictive Capabilities. *Res Mech.* 1981;3:175–93.
- [55]. Ashby MF, Frost HJ. Deformation-mechanism maps: the plasticity and creep of metals and ceramics. Oxford Pergamon Press Ltd; 1982.
- [56]. Kroner E. On the plastic deformation of polycrystals. *Acta Metall.* 1961;9:155–61.
- [57]. Budiansky B, Wu TT. Theoretical prediction of plastic strains of polycrystals. *Proc 4th Congr. Appl. Mech.* 1962. p. 1175–85.
- [58]. Foreman AJE, Makin MJ. Dislocation movement through random arrays of obstacles. *Philos. Mag.* 1966;14:911–24.
- [59]. Argon AS. Strengthening Mechanisms in Crystal Plasticity. Oxford University Press; 2008.
- [60]. Ashby MF. The theory of the critical shear stress and work hardening of dispersion-hardened crystals. Defense Technical Information Center, UK; 1966.
- [61]. Nes E, Marthinsen K, Brechet Y. On the mechanisms of dynamic recovery. *Scr. Mater.* 2002;47:607–11.

- [62]. Aplin PF, Angelo DD. Dislocation-creep mechanisms in Type 316 steel. In: Wilshire B, Evans RW, editors. *Creep Fract. Eng. Mater. Struct.* Institute of Metals, London; 1990. p. 537–45.
- [63]. Gerland M, Violan P. Cyclic Hardening and Dislocation Structures in Type 316 Stainless Steel at 600°C. *Mater. Sci. Eng.* 1986;84:23–33.
- [64]. Kestenbach H-J, Krauss W, Silviera TL da. Creep of 316 Stainless Steel under High Stresses. *Acta Metall.* 1978;26:661.
- [65]. Mathew MD, Sundararaman M, Mannan SL. Dislocation Substructure and Precipitation in Type 316 Stainless Steel Deformed in Creep. *Mater. Trans.* 1997;38:37–42.
- [66]. Neves S, Santos F, Anacleto W, Paulo L. Creep Parameters and Dislocation Substructure in AISI 316 Austenitic Stainless Steel From 600°C to 800°C. *Mater. Res.* 2017;20:1–5.
- [67]. Mamun AA. Origin of creep-fatigue back stress and its effect on deformation and damage. The Open University; 2016.
- [68]. Li DF, O'Dowd NP, Davies CM, Zhang SY. Microscale prediction of deformation in an austenitic stainless steel under uniaxial loading. *Eur. J. Mech. A/Solids*. Elsevier Ltd; 2011;30:748–60.
- [69]. Lai J. A study of precipitation in AISI type 316 stainless steel. *Mater. Sci. Eng.* 1983;58:195–209.
- [70]. Shelton EFJ. HTBASS Creep understanding. Re-priming of creep deformation behaviour during cyclic loading. 2017.
- [71]. NIMS. Metallographic atlas of long-term crept materials - SUS 316H TB. 2003.
- [72]. Wilshire B, Willis M. Mechanisms of Strain Accumulation and Damage Development during Creep of Prestrained 316 Stainless Steels. *Metall. Mater. Trans. A.* 2004;35:563–71.
- [73]. Yamada H, Li C-Y. Stress relaxation and mechanical equation of state in austenitic stainless steels. *Metall. Trans.* 1973;4:2133–6.
- [74]. Bachmann F, Hielscher R, Schaeben H. Grain detection from 2D and 3D EBSD data - Specification of the MTEX algorithm. *Ultramicroscopy*. 2011;11:1720–33.
- [75]. Addleman RL, Webster GA. A simple model of uniaxial creep recovery and stress relaxation based on residual-stress redistribution. *J. Strain Anal. Eng. Des.* 1973;8:99–107.
- [76]. Henderson BJ, Snedden JD. Creep recovery of commercially pure copper. *J. Mech Eng Sci.* 1968;10:24–35.



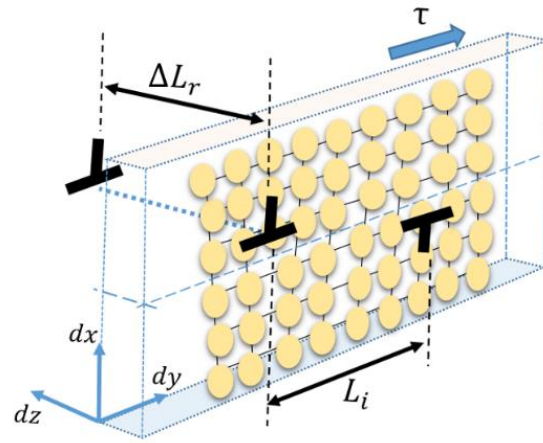


Figure 3. Schematic of annihilated dislocation dipole segment length, ΔL_r . The spacing between segments, L_i , is related to the accumulated dislocation junction obstacle density.

	Room temperature (short-term plasticity)	High temperature (long-term creep)	
Forest dislocations	glide, multiplication	glide, multiplication + climb, recovery	
Precipitation	Orowan bowing + enhanced dislocation multiplication	Orowan bowing + climb bypassing (nucleation, growth, coarsening)	EX / ST
Solid solution	constant resistance (Solute strengthening)	Solute strengthening + solute drag Depletion by precipitation	ST Only
Dislocations (cyclic)	Dynamic recovery (annihilation)		

Figure 4. Current state of the micromechanical model employed for EX and SA 316H material. Solution treated (ST) 316H stainless steel is not examined in the present study.

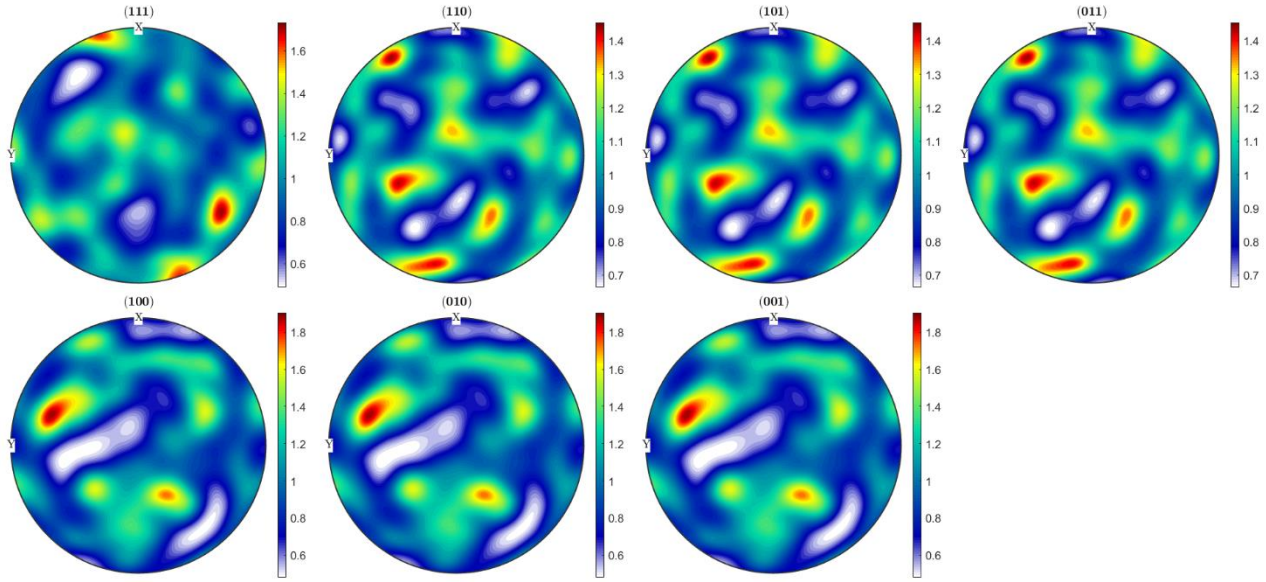


Figure 5. Pole figures of initial texture - ex-service 316H material considered (100 grains). Pole figures are generated using the MTEX open-source software [74].

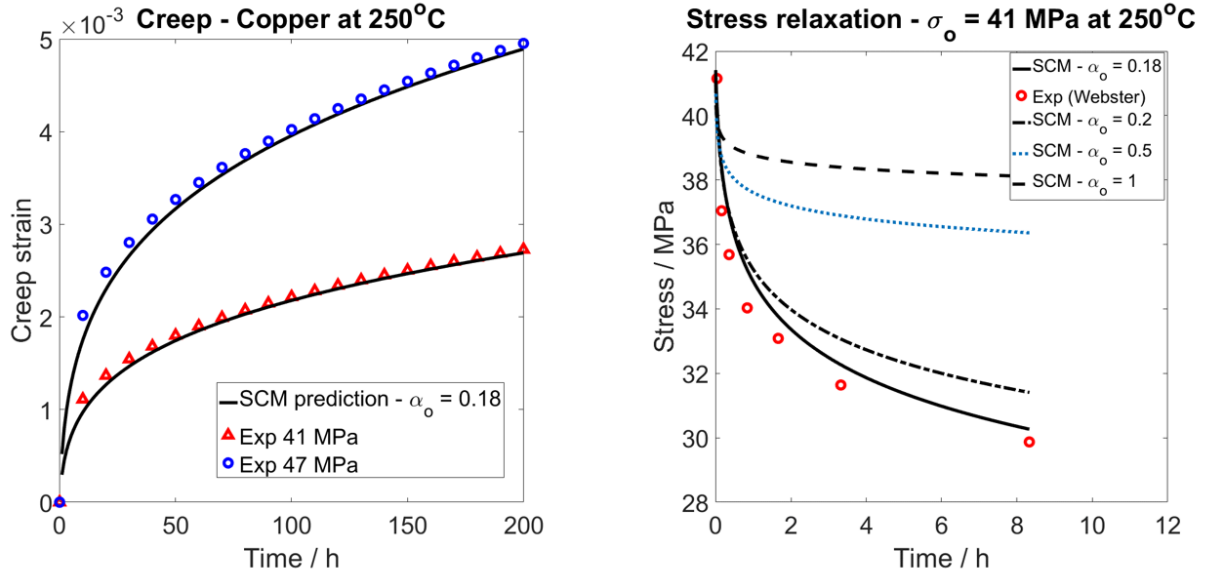


Figure 6. Creep and relaxation model predictions with α_0 for Cu at 250°C. Data after [75,76].

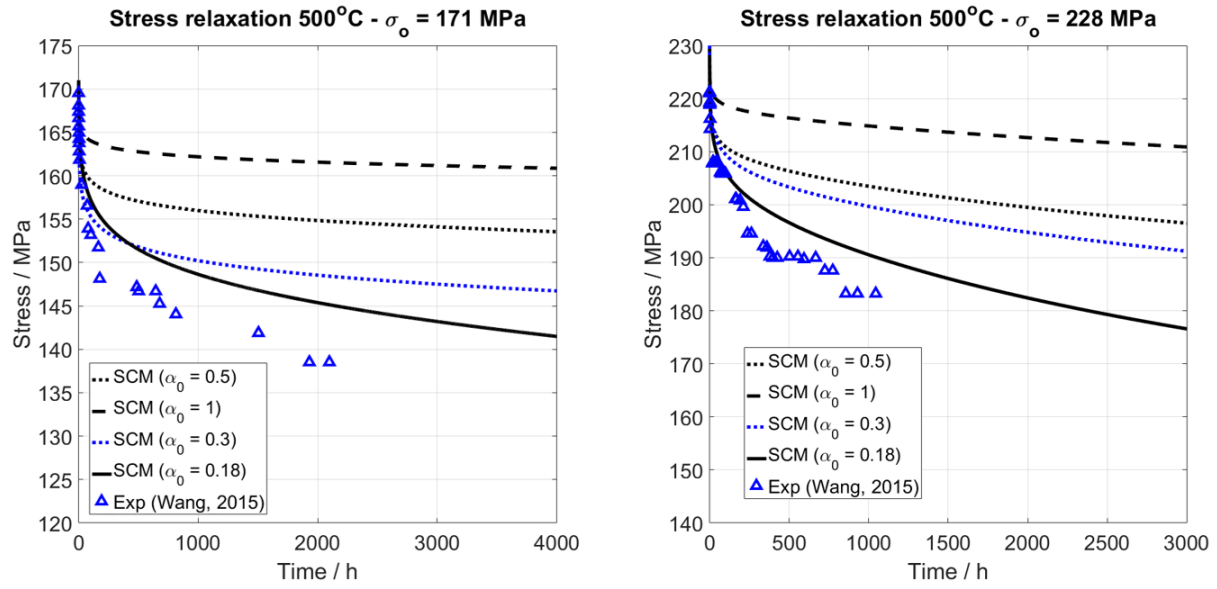


Figure 7. Stress relaxation model predictions and experimental results, EX 316H at 500°C.

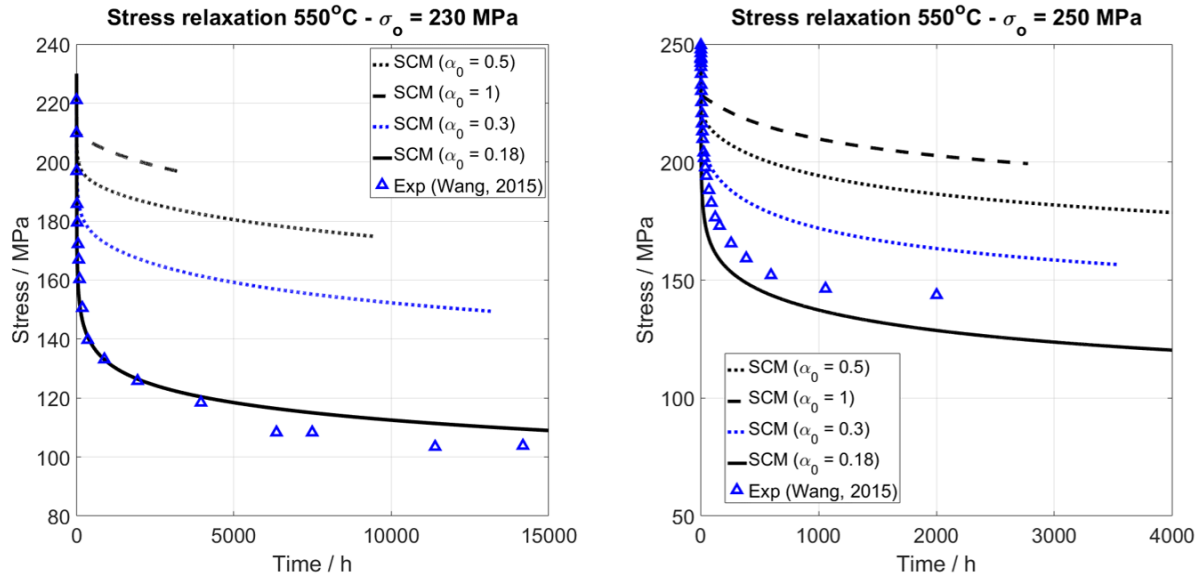


Figure 8. Stress relaxation model predictions and experimental results, EX 316H at 550°C.

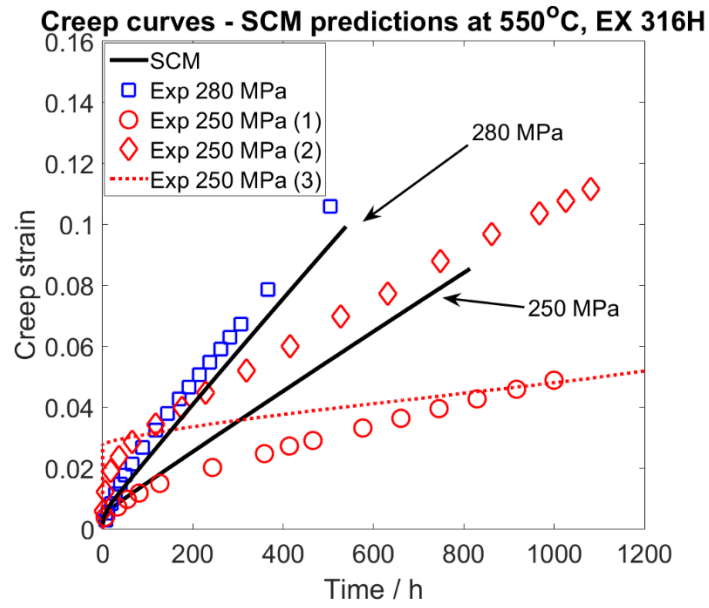


Figure 9. Examples of forward creep predictions – macroscopic creep strain with time for EX 316H at 550°C, $\alpha_0 = 0.18$. The set of parameters used to fit the forward creep curves at certain temperature and constant stress are then used to predict the relaxation response at that temperature and initial stress. Experimental data after EDF Energy.

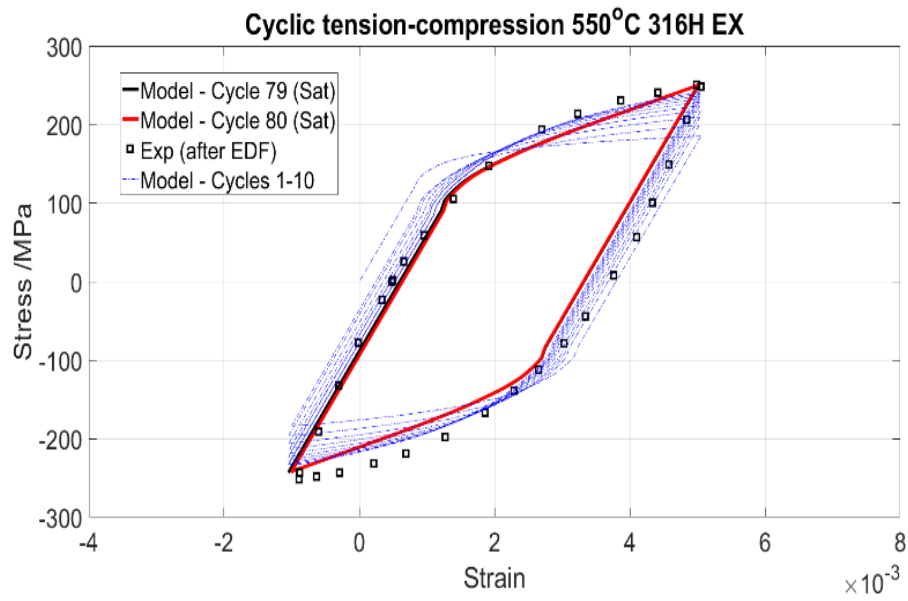


Figure 10. Saturated stress-strain curve after 80 cycles – SCM prediction and experiments ex-service 316H at 550°C. Experimental data provided by EDF Energy.

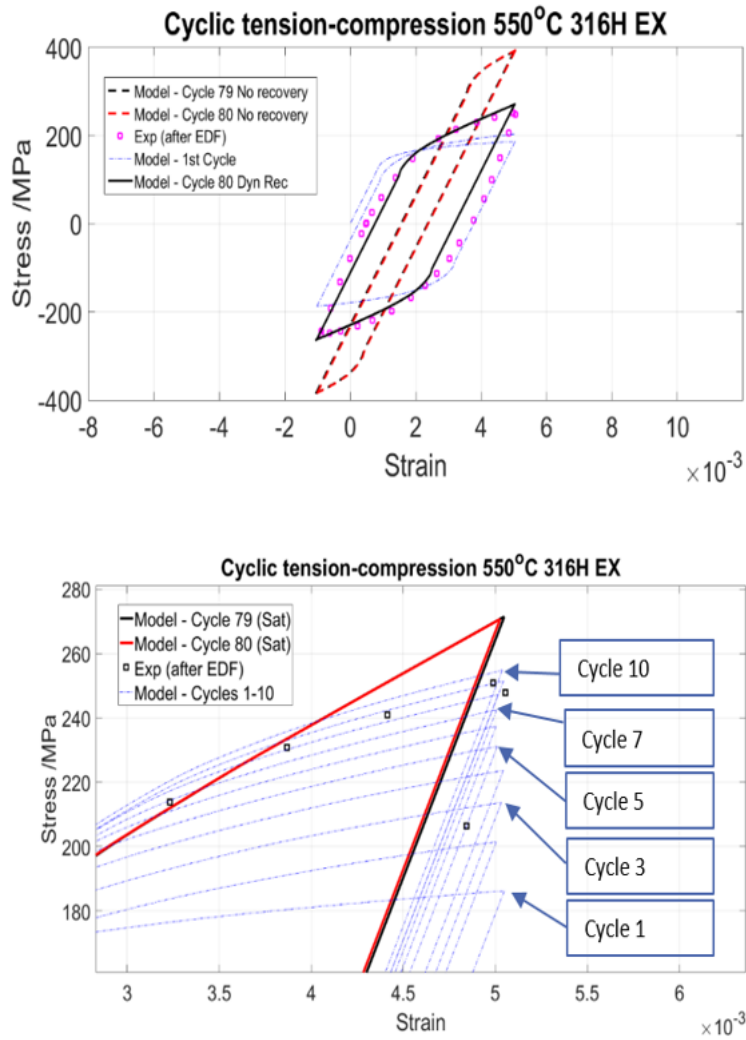


Figure 11. Left: Saturated stress-strain curve after 80 cycles – SCM prediction with and without the model of dynamic recovery, 316H at 550°C. Right: Increase of the effect of dynamic recovery with the first 10 cycles on the macroscopic response, close-up of stress-strain curve.

Cyclic tension-compression 250°C Commer Pure Cu

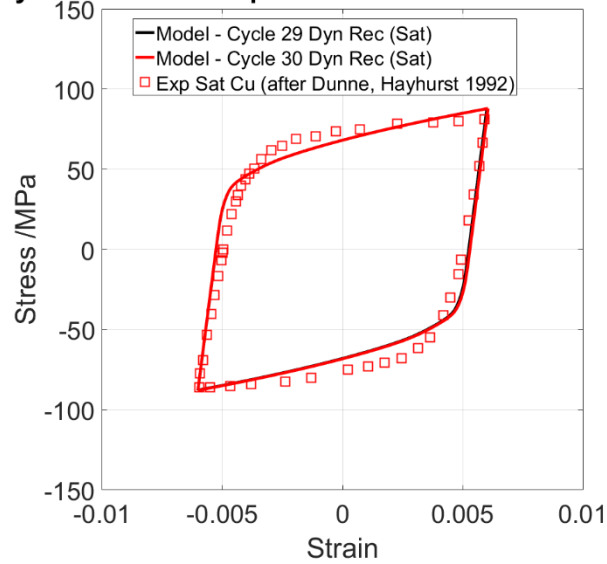


Figure 12. Saturated stress-strain curve after 30 cycles – SCM prediction and experiments, Cu at 250°C. Experimental data after [14].

Cyclic tens-compr - $\epsilon_t = 0.4\%$ dwells 550°C 316H EX

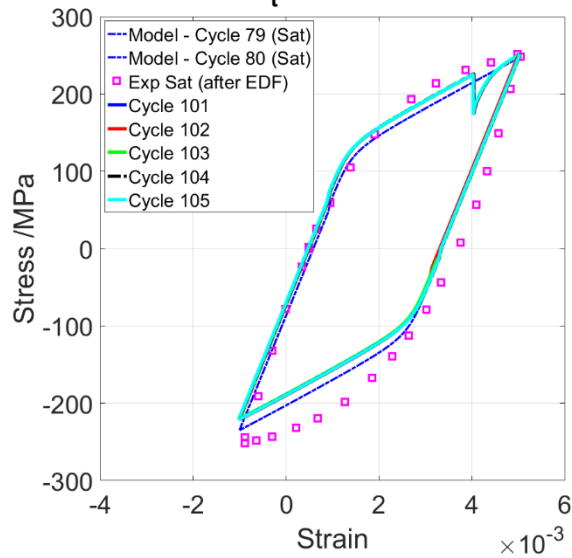


Figure 13. Model prediction of stress-strain curve for same strain dwell history – 316H at 550°C.

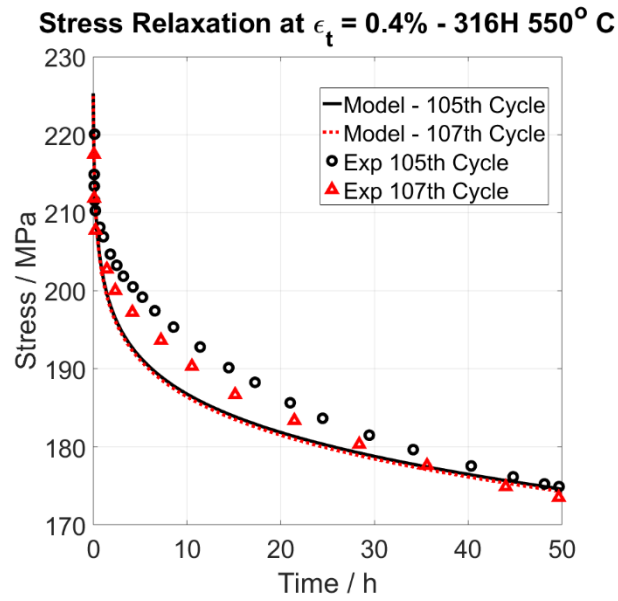


Figure 14. Model prediction and experimental data from [44] – relaxation at $\epsilon_t = 0.4\%$ after 105th and 107th cycle, 316H at 550°C.

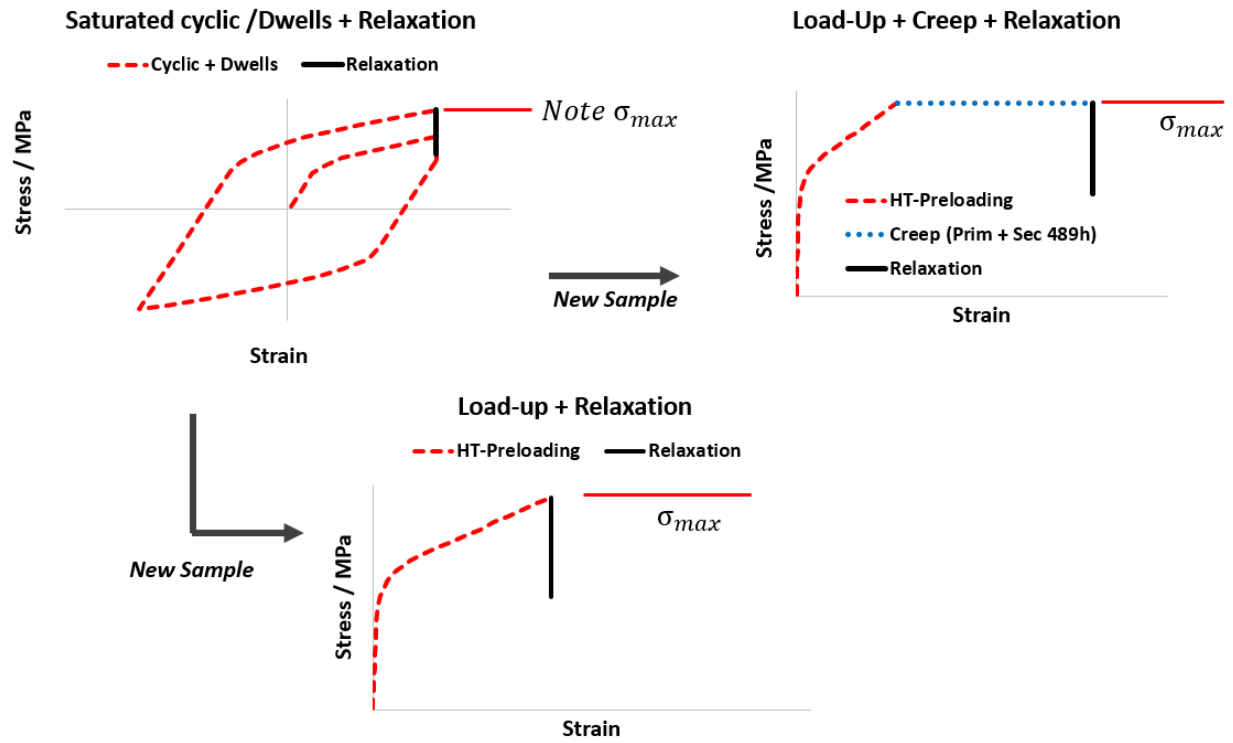


Figure 15. Schematic of the Type 2 load histories considered.

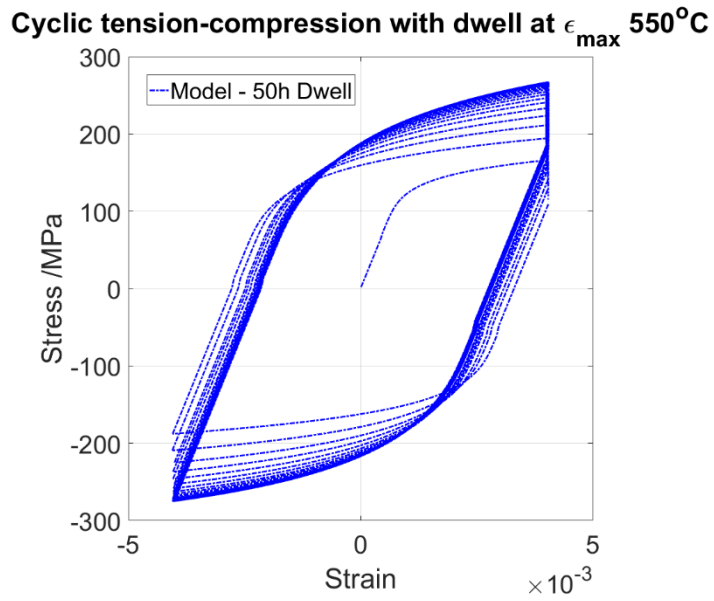


Figure 16. SCM predictions of cyclic stress-strain curve with dwells – Type 2 history, 316H at 550°C and $\Delta\epsilon = 0.8\%$.

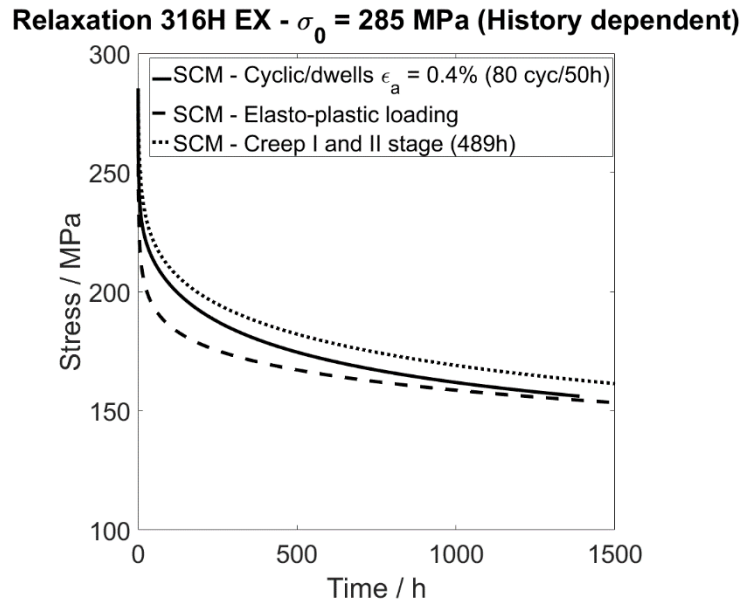


Figure 17. Model predictions of long-term relaxation behaviour for Type 2 sub-histories – 316H at 550°C.

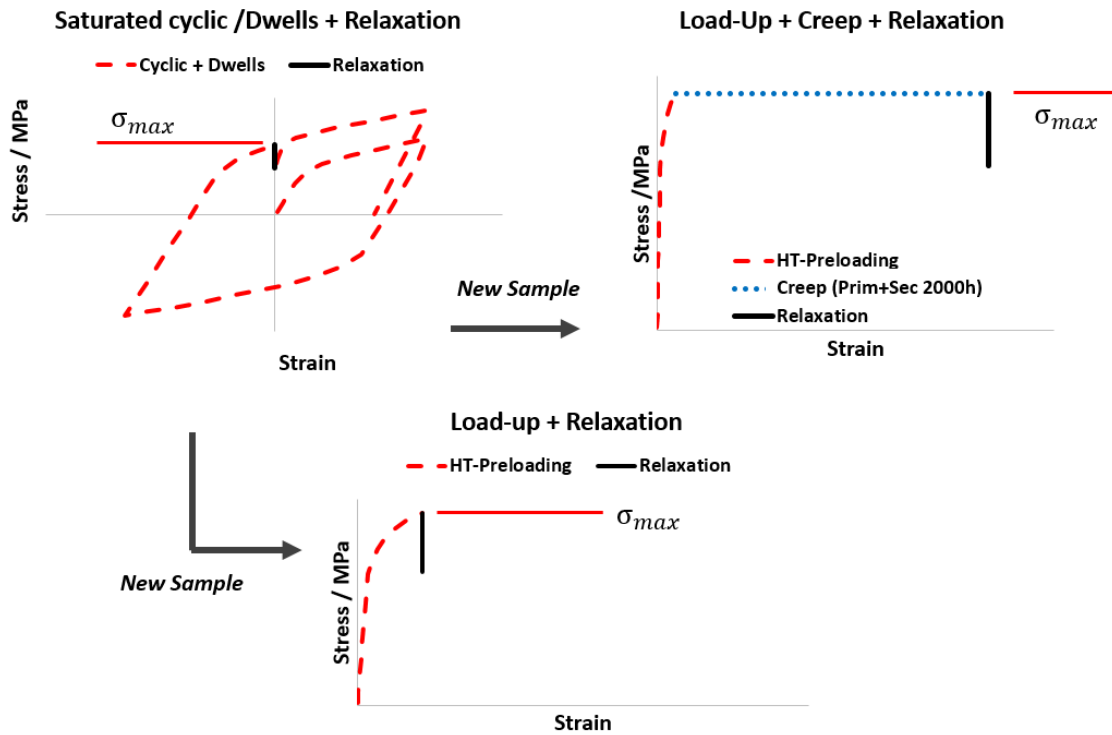


Figure 18. Schematic of the Type 3 load histories considered.

Relaxation 316H EX - $\sigma_0 = 199$ MPa (History dependent)

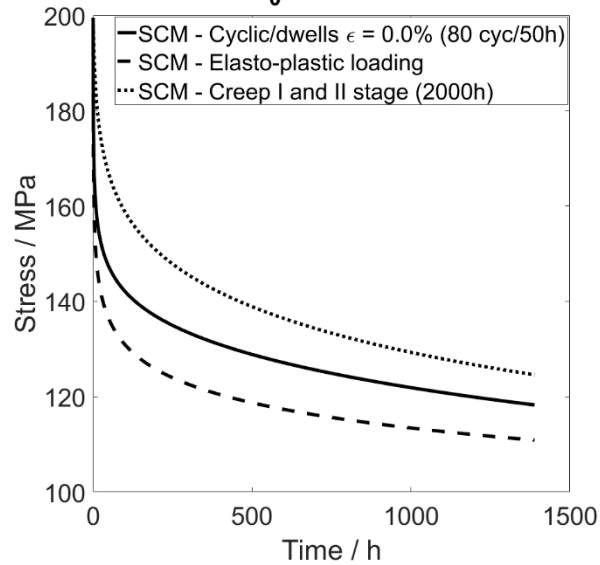


Figure 19. Model predictions of long-term relaxation behaviour for Type 3 sub-histories – 316H at 550°C.

Stress drop 316H EX - After 1st and Saturated Cycle (History dep)

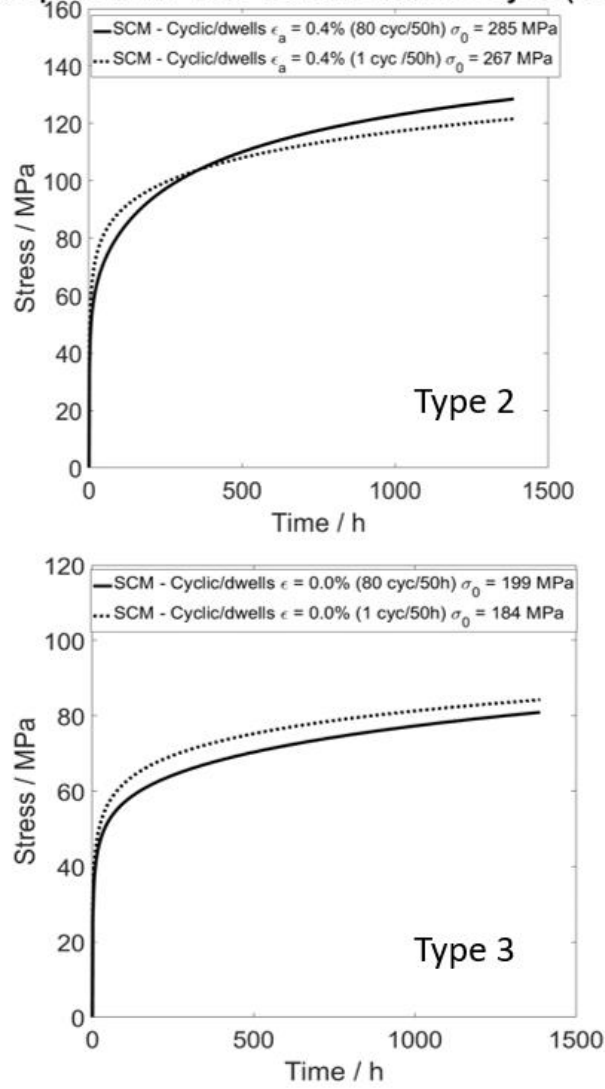
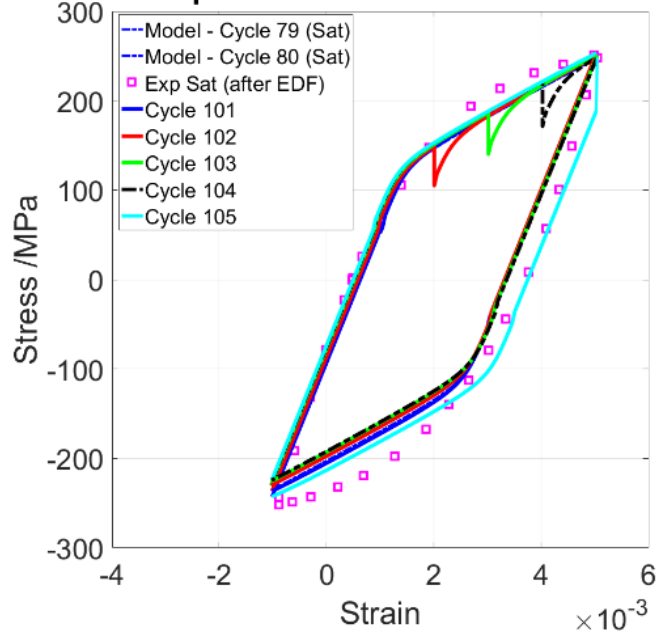


Figure 20. Comparison between model predictions of relaxation after 1 and 80 cycle-dwells for Type 2 and 3 histories, 316H at 550°C, $\Delta\epsilon = 0.8\%$.

Cyclic tens-compr - different strain dwells 550°C 316H EX



Exp cyclic with dwells - 316H 550°C - EDF

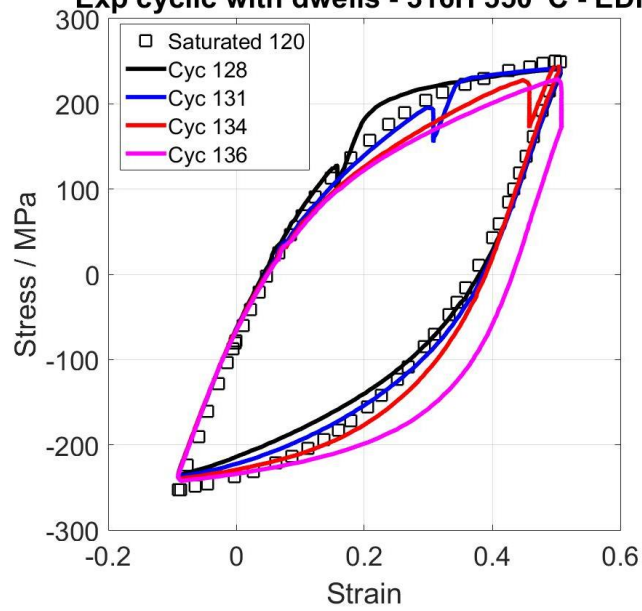


Figure 21. Top: Model prediction of stress-strain curve for different strain dwell history – 316H at 550°C. Bottom: Experimental stress-strain curve towards the 136th cycle [44] in intervals of 0.05%.

Relaxation dwells (50h) Cycles 105,107 and 108 - 316H

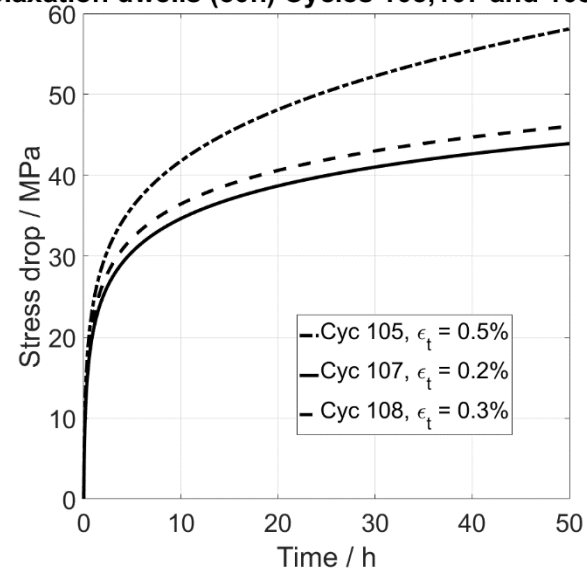


Figure 22. Relaxation at different strain levels and cycles – model prediction, 316H at 550°C.

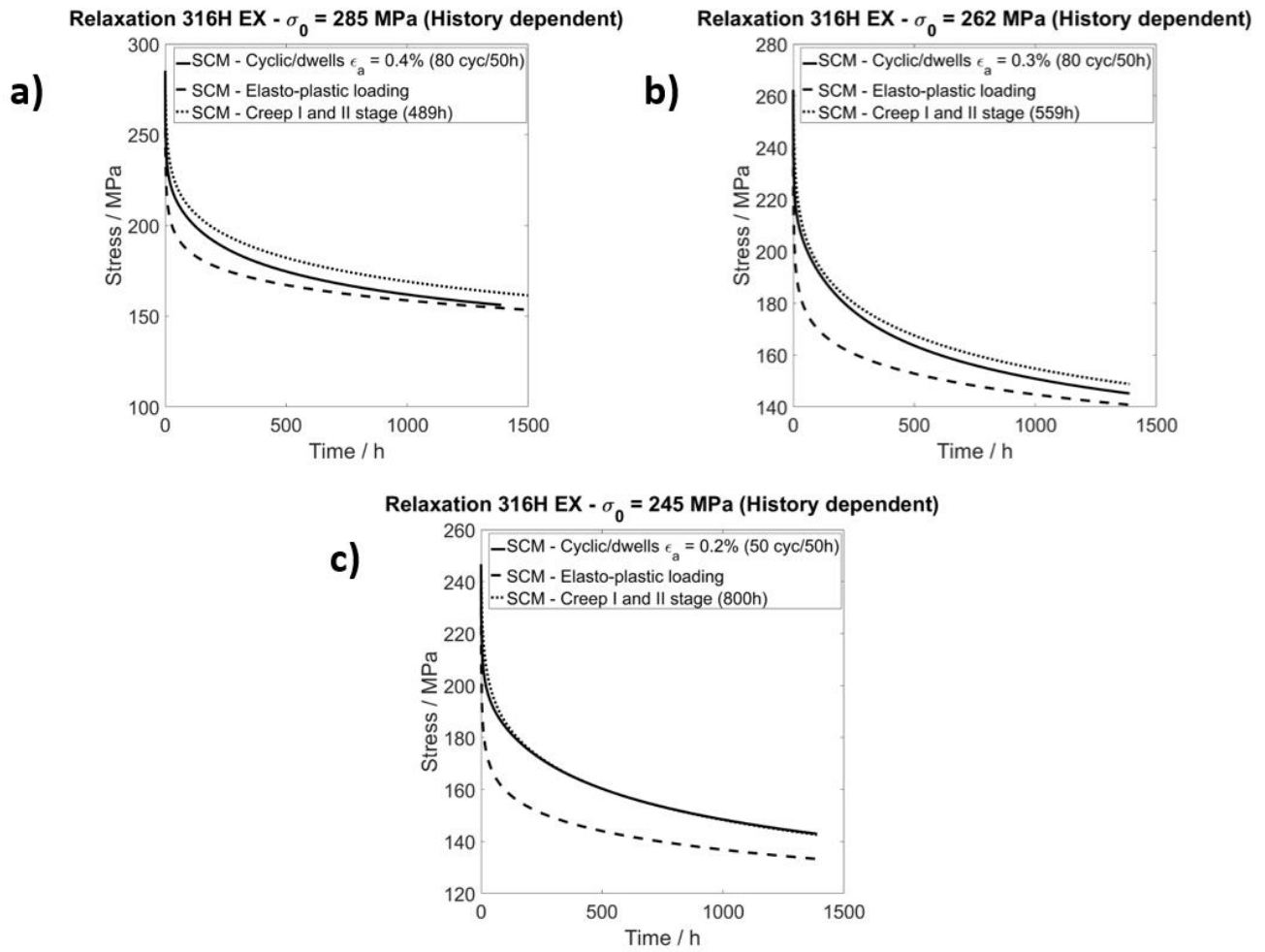


Figure 23. Model prediction of long-term relaxation behaviour for Type 2 sub-histories, prior cycling at a) 0.8%, b) 0.6% and c) 0.4% strain range – 316H at 550°C.

Stress drop 316H EX - Strain-range dependence

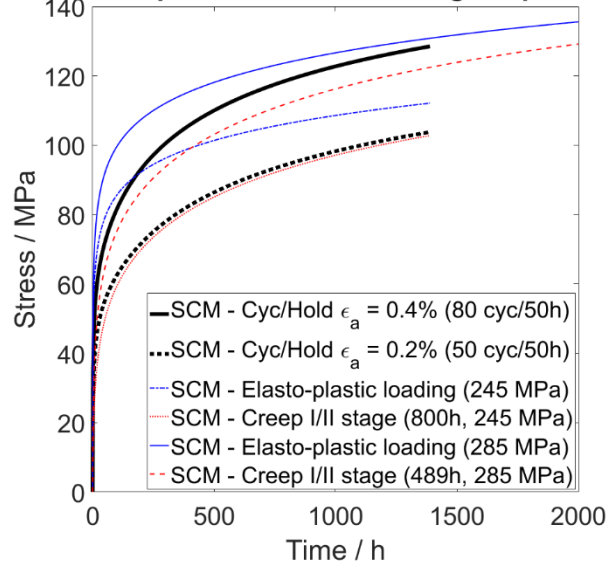
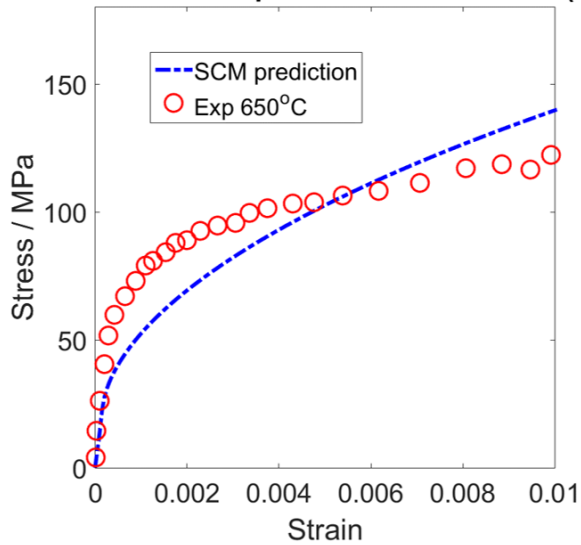


Figure 24. Long-term stress drops during relaxation behaviour for Type 2 sub-histories, prior cycling at 0.8% and 0.4% strain range – 316H at 550°C.

Stress-strain response at 650°C - 316H (ST)



Cyclic tension-compression 650°C 316H (ST)

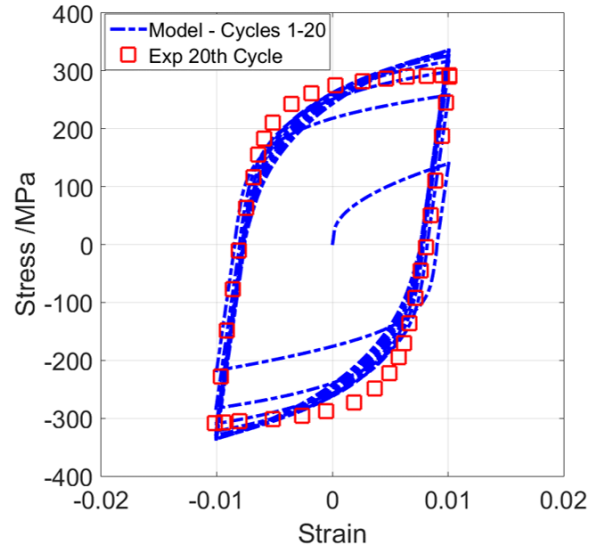


Figure 25. SCM predictions of elastic-plastic deformation behavior and cyclic stress-strain curve at 650°C. Calibration against experimental data from [67].

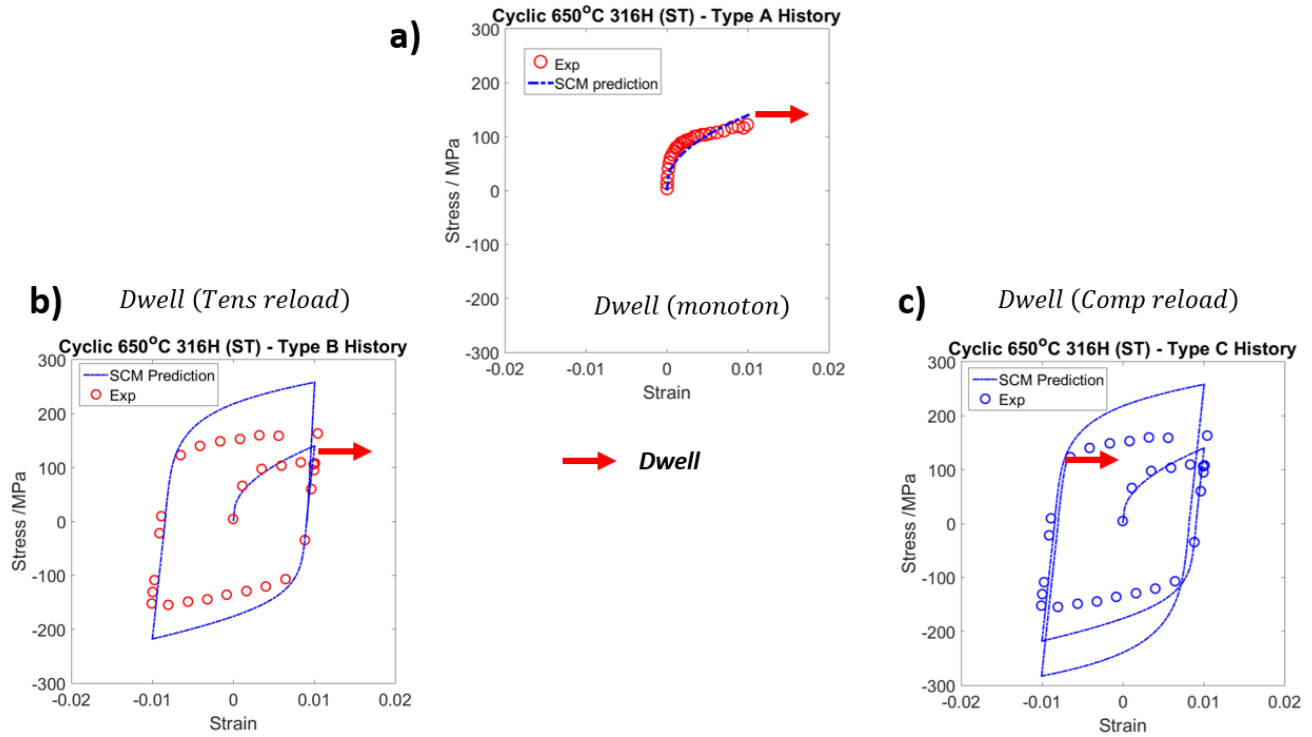


Figure 26. Experimental data [67] and modelling predictions of cyclic-creep dwell histories for each specimen – a) Specimen A, b) Specimen B and c) Specimen C. Positions of tensile creep dwells are illustrated by red arrows.

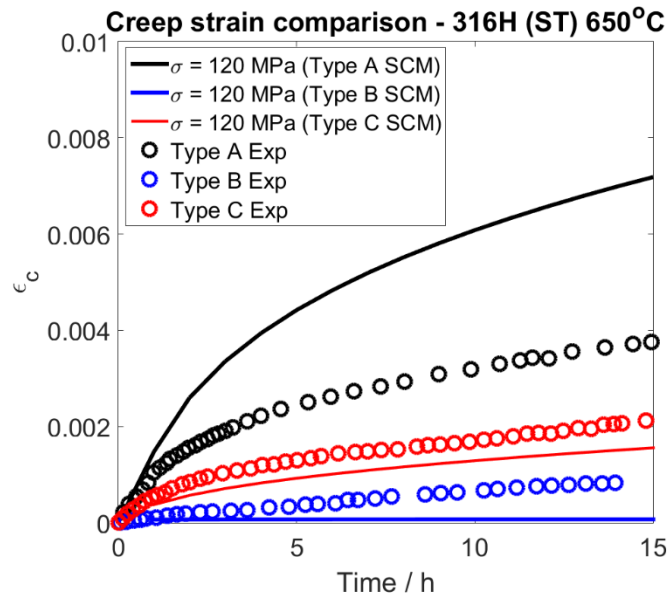


Figure 27. SCM predictions of creep strain accumulation vs time for Specimen A-C at 650°C and 120 MPa. Results are compared against experimental data from [67].

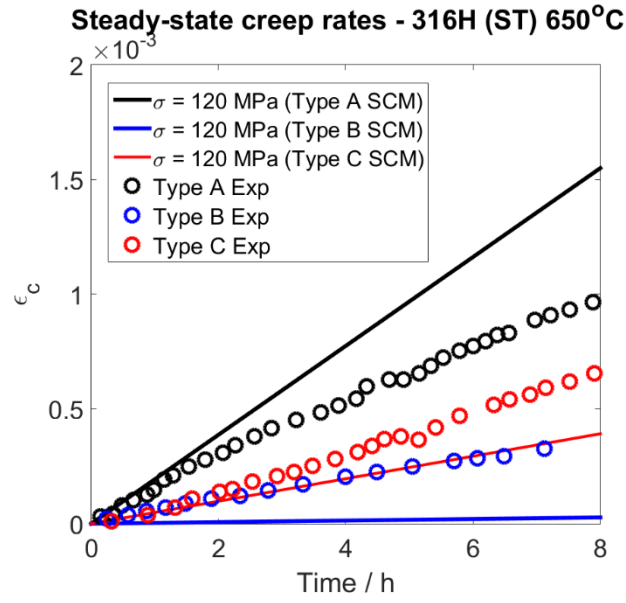


Figure 28. SCM predictions of minimum creep strain rates for Specimen A-C at 650°C and 120 MPa. Results are compared against experimental data from [67]. N.B. The prediction for Specimen B agrees qualitatively with the experimental response, however, the moderate constant stress level and the compatible stress field in Specimen B could influence the creep response and underestimate the strain rate.